Armadillo repeat-containing kinesin represents the versatile plus-end-directed transporter in plants

Mari W. Yoshida[1], Maya Hakozaki [1], and Gohta Goshima[1,2*]

1. Department of Biological Science, Graduate School of Science, Nagoya University, Nagoya 464-8602, Japan

2. Sugashima Marine Biological Laboratory, Graduate School of Science, Nagoya University, Toba 517-0004, Japan

*To whom correspondence should be addressed. Email: goshima@bio.nagoya-u.ac.jp

Author contributions: M.W.Y. and G.G. designed the research; M.W.Y. performed the experiments and analysed the data; M.W.Y. and M.H. selected the transgenic lines; M.W.Y. and G.G. wrote the paper.

Abstract

Kinesin-1, also known as conventional kinesin, is widely utilised for microtubule plus-end-directed ("anterograde") transport of various cargos in animal cells. However, a motor functionally equivalent to the conventional kinesin has not been identified in plants, which lack the kinesin-1 genes. Here, we show that plant-specific armadillo repeat-containing kinesin (ARK) is the long sought-after versatile anterograde transporter in plants. In *ARK* mutants of the moss *Physcomitrium patens*, the anterograde motility of nuclei, chloroplasts, mitochondria, and secretory vesicles was suppressed. Ectopic expression of non-motile or tail-deleted ARK did not restore organelle distribution. Another prominent macroscopic phenotype of *ARK* mutants was the suppression of cell tip growth. We showed that this defect was attributed to the mislocalisation of actin regulators, including RopGEFs; expression and forced anterograde transport of RopGEF3 suppressed the growth phenotype of the *ARK* mutant. The mutant phenotypes were partially rescued by ARK homologues in *Arabidopsis thaliana*, suggesting the conservation of ARK functions in plants.

Key words

Kinesin/Microtubule-based transport/Cell tip growth/Actin/*Physcomitrium (Physcomitrella) patens*

Introduction

The proper positioning of cellular components in the cytoplasm is critical for cell physiology. It is particularly important for highly polarised cells, such as neurons and epithelial cells, in animals. Regulated bidirectional transport on microtubules is a major mechanism for positioning intracellular components and requires motor proteins that bind to cargo and walk on microtubules [1–3]. In animal cells, cytoplasmic dynein is responsible for the majority of minus-end-directed (retrograde) transport in the cytoplasm, and a few kinesin family members have been identified as plus-end-directed (anterograde) transporters [1]. Among them, kinesin-1, also called conventional kinesin, is a universal transporter whose critical roles have been identified in various cell types [4–6]. Cargos of kinesin-1 include giant organelles, such as nuclei and mitochondria, as well as smaller

cellular components, such as secretory vesicles, protein complexes, and RNA granules [7–10,10,11]. These anterograde and retrograde transporters work together on the same cargo to allow bidirectional transport [12,13].

Intriguingly, plants do not possess cytoplasmic dynein or conventional kinesin. Intracellular transport in plants has long been believed to be predominantly driven by myosin and actin. Cytoplasmic streaming is the best-studied phenomenon observed in many plant cell types and is powered by myosin motors [14,15]. Furthermore, in *Arabidopsis thaliana* root hair, myosin XI-i transports the nucleus to the centre of the growing cell [16]. Chloroplast photo-relocation, a phenomenon in which chloroplasts are repositioned in response to light stimuli, is also promoted by specific chloroplast-associated actin filaments that polymerise between the plasma membrane and the chloroplasts in *A. thaliana* [17]. However, the microtubule-dependent motility of cellular components also exists in plants. For example, nuclear movement requires microtubules in meristemoid mother cells in *A. thaliana* and microspores in *Nicotiana tabacum* [18,19]. In the former case, nuclear positioning affected stomatal patterning, suggesting the physiological importance of microtubule-dependent nuclear migration. A series of studies using protonemal tissue of the moss *Physcomitrium patens* (formerly called *Physcomitrella patens*) have also revealed the contribution of microtubules and motors to organelle transport. The tip-growing apical cell of *P. patens* protonema is an ideal system for studying microtubule-dependent bidirectional transport, as ~90% of the microtubules are oriented in such a manner that the plus ends face the cell tip during interphase [20]. In this system, when plus-end-directed motility is predominant over minus-end-directed motility, the organelle moves apically and is abundant on the apical side, and vice versa. Based on this advantage, several kinesin-14 family members have been identified as the drivers of retrograde transport, namely KCH for the nucleus, KCBP for the chloroplast and telophase chromosome, and ATK for newly-formed microtubules [21–23]. Studies in *P. patens* thus drew a functional analogy between kinesin-14s and dynein and further illustrated the contribution of intracellular transport driven by the microtubule-kinesin mechanism.

Anterograde transporter is a missing piece in the model of intracellular transport in plants. Plant genomes do not encode proteins paralogous to kinesin-1, which is characterised by a unique domain in its tail that binds to the light chain [24]. Kinesin-3 is another potent cargo transporter in animal cytoplasm, and it is best known as a synaptic vesicle transporter in neurons [25,26]. However, this subfamily is also missing in plants; thus, no deduction can be made from genome sequences regarding the identity of the versatile anterograde transporter in plants. Nevertheless, armadillo repeat-containing kinesin (ARK), which constitutes a subfamily unique to the plant lineage, could be a candidate motor protein. In a previous study, we observed that the nucleus was not properly positioned after inducing RNAi that targeted two of the four *ARK* genes in moss protonemata [27]. However, whether ARK is a genuine transporter of the nucleus could not be clarified. Although the purified ARKb motor can glide microtubules in the conventional *in vitro* gliding assay (i.e. motor activity is present), the motility of ARKb-Citrine on the microtubules *in vivo* could not be observed [27]. This contrasts with the observation that retrograde transporters show fast (~400 nm/s) and long (~1 μm) minus-end-directed motility *in vivo* [21,28]. Furthermore, AtARK1, the most-studied ARK, is localised to the plus end of microtubules, triggers microtubule catastrophe [29], and tethers

the ER to the microtubule end by binding to the ER-shaping protein atlastin GTPase RHD3 [30]. Alterations in microtubule dynamics can, in principle, affect nuclear motility, as shown in yeast [31]. However, none of these previous studies have clarified the mechanism by which ARK positions nuclei.

This study initially aimed to elucidate how ARK proteins position the nuclei. Surprisingly, in the newly established *ARK* mutant lines, microtubule plus-end-directed motility of not only the nuclei but also chloroplasts, mitochondria, and secretory vesicles was suppressed. Ectopic expression of a non-motile mutant or tail-deleted ARK did not restore organelle distribution. Furthermore, when a brighter fluorescent protein, mNeonGreen (mNG), was attached to the endogenous ARKb, processive motility towards the microtubule plus ends was observed *in vivo*. The most prominent macroscopic phenotype of *ARK* mutants was the suppression of cell tip growth, which is known to require the actin cytoskeleton. Interestingly, this defect was attributed to the mislocalisation of actin regulators, including the guanine nucleotide exchange factors (GEFs) of Rho-type GTPases. These phenotypes were partially rescued by the ectopic expression of ARK homologues in *A. thaliana*. The results suggest that ARK is a conserved and versatile anterograde transporter in plants.

Results

P. patens ARK is required for protonemal growth

Four highly homologous genes have been identified in the ARK family of moss (Fig. 1A). Previously, we examined the RNAi knockdown mutant of *ARK* and identified a specific defect in protonemal apical cells, namely, nuclear mispositioning [27]. The RNAi targeted *ARKa* and *ARKb* genes and reduced their mRNA levels by ~50%, whereas ARKc and ARKd were kept intact, which might have prevented the expression of several potential phenotypes. To isolate multiple loss-of-function mutants of *ARK*, we used CRISPR/Cas9 [32,33]. We attempted to simultaneously introduce a frameshift just before the critical, conserved ATPase motif or microtubule-binding site in the motor domain of *ARKa-d*, which would destroy its motor activity [34]. We used two parental lines, which expressed mCherry-α-tubulin and GFP-α-tubulin/Histone2B-mCherry. Consequently, we obtained independent mutants containing a variety of mutations in different gene sets from both backgrounds. Overall, all the isolated single- and double frame-shifted lines (*a*, *b*, *ab*, *ad*, *bc*, and *bd*) showed no or only mild growth defects (Fig. S1A). In contrast, the colony sizes of the triple (*abc*) and quadruple (*abcd*) mutants were dramatically smaller than those of the parental line (Fig. 1B, C, S1A). One line, called Δ*ARKabcd*, possessed frameshift mutations in all the *ARK* genes (GFP-α-Tubulin/Histone2B-mCherry background), whereas the other, Δ*ARKabc*, had deletions in *ARKa, ARKb,* and *ARKc* but *ARKd* remained intact (mCherry-α-tubulin background) (Fig. S1B). These two lines were chosen for further analyses.

The protonemal tissue was underdeveloped in Δ*ARKabc* and Δ*ARKabcd*. The phenotype was more severe in Δ*ARKabcd* than Δ*ARKabc*, and gametophore tissue (leafy shoot) predominated in the colony (Fig. 1B, top row). The morphology of the Δ*ARKabc* gametophore was normal, but twisted leaves consisting of abnormally shaped cells were observed in Δ*ARKabcd* (Fig. 1B, third and fourth rows). In addition, Δ*ARKabc* and Δ*ARKabcd* developed fewer and shorter rhizoids (root-like filamentous outgrowths) than

135 the parental lines (Fig. 1B, red arrowheads).
136 To confirm that the observed phenotype was derived from the disruption of the *ARK*
137 genes, we performed a rescue experiment in which the ARKb-mNeonGreen (mNG)
138 transgene was ectopically expressed in the mutants. We failed to transform the construct
139 into Δ*ARKabcd* in multiple attempts; sufficient numbers of viable protoplasts for
140 transformation could not be obtained from this extremely unhealthy line. In contrast,
141 Δ*ARKabc* was transformable and a transgenic line stably expressing ARKb-mNG was
142 established. The colony growth of this line was restored, indicating that the protonemal
143 growth defect was caused by a reduction in ARK protein levels (Fig. 1B, C). To determine
144 whether the growth defect was associated with the motor activity of ARKb, we
145 constructed a "rigor" mutant of ARK (ARKb (T169N) -mNG), which binds to
146 microtubules but does not show motility [35]. We observed that protonemal colony growth
147 was not rescued by the expression of this mutant ARK (Fig. 1B, C). These results indicate
148 that ARKs with intact motor activity are, likely redundantly, required for protonemal and
149 rhizoid growth as well as gametophore development.
150
151 **ARK is required for intracellular transport of the nucleus, chloroplast,**
152 **mitochondrion, and secretory vesicle**
153 We next performed time-lapse fluorescence microscopy on the *ARK* mutants,
154 focusing on nuclear motility. The underdevelopment of the protonemal tissue prevented
155 us from imaging and analysing the long-distance motility of organelles in Δ*ARKabcd*.
156 Therefore, Δ*ARKabc* which showed less severe protonemal growth defects, was used for
157 the cellular analysis. Consistent with the results of a study using *ARKa/b* RNAi [27], the
158 nucleus moved basally after anaphase and was located adjacent to the basal cell wall in
159 the apical cells of Δ*ARKabc* (Fig. 2A, B; nuclei can be identified as an area devoid of
160 mCherry-α-tubulin signals in each z-slice). Like the control cells, the mispositioned
161 nuclei in the mutant cells also showed apical movement during mitotic prophase (Fig. 2B;
162 -60~0 min). However, because of the overly basal localisation of the nucleus during
163 interphase, mitotic spindle formation occurred more basally than in the control line (Fig.
164 2C). The mispositioning of the spindle was more drastic than that observed in the previous
165 *ARKa/b* RNAi line [27], suggesting that the previous RNAi line represented a weaker
166 hypomorphic allele. Importantly, the position of the nucleus and spindle was largely
167 rescued by ectopic expression of ARKb-mNG but not by that of the rigor mutant,
168 indicating that the nuclear mispositioning was associated with the loss of ARK motor
169 activity (Fig. 2B, C).
170 The constant, rapid, and bidirectional motility of chloroplasts during the normal cell
171 cycle is dependent on microtubules, and KCBP kinesin (kinesin-14VI) drives their
172 retrograde transport [22]. However, the factor(s) responsible for anterograde movement (i.e.
173 plus-end-directed transporters) remains unknown. During imaging, we realised that
174 chloroplasts in the mutant behaved differently from those in the control line. In Δ*ARKabc*,
175 chloroplasts moved basally overall and clustered near the basal cell wall in the apical cell
176 (Fig. 2A, D, E, Movie 1). This behaviour was opposite to that of the *KCBP* knockout line,
177 in which chloroplasts were predominantly moved to and observed on the apical side of
178 the cell [22]. This phenotype was also rescued by ectopic expression of ARKb-mNG but
179 not by the rigor mutant (Fig. 2A, E). These results indicate that the bidirectional motility
180 of the chloroplast is driven by KCBP (retrograde) and ARK (anterograde).

To the best of our knowledge, ARK is the first anterograde kinesin to be identified as a participant in the movement of multiple organelles in plant cells. This led us to hypothesise that ARK may be a versatile anterograde motor for many cargos, similar to conventional kinesin in animals. To test this possibility, we analysed the mitochondrion, another giant membranous organelle possessing DNA. To visualise the mitochondria, the mitochondrial membrane protein γ-F1ATPase-mNG was expressed in wild-type and Δ*ARKabc* (note that Δ*ARKabcd* is not amenable to transformation). Mitochondria showed bidirectional movement along cytoplasmic microtubules; however, most of them translocated apically from their initial positions in the control line after tracking for 6 min (65 of 72 mitochondria in six cells; Fig. 3G). In contrast, more basal translocation was observed in Δ*ARKabc* (38 of 72 mitochondria in six cells). These results suggest that ARK is involved in the plus-end-directed transport of mitochondria.

Next, we focused on secretory vesicles, which are also known cargos of kinesin-1 and kinesin-3 in animals [1]. In *P. patens,* actin-based motor myosin XI transports RabE14-positive vesicles near the cell apex [36]. Whether microtubules and kinesins are involved in vesicle transport remains unknown. Referring to the literature on *Arabidopsis* [37], we labelled vesicles by tagging endogenous RabA2b with mNG in the wild-type and Δ*ARKabc* lines. RabA2b is a small GTPase homologous to Rab-A2 in *A. thaliana*, which regulates the secretory pathway by recruiting SNARE proteins [38]. In the control line, the mNG-RabA2b signal accumulated at the apex (Fig. 3A). Time-lapse imaging using a spinning-disc confocal microscope identified motile small puncta. When we focused on long-distance movement of the puncta toward the cell tip (i.e. plus-end-directed motility), we observed that it was markedly suppressed when the microtubules or actin were depolymerised by latrunculin A or oryzalin (Fig. 3C). Thus, both actin- and microtubule-dependent mechanisms are responsible for the long-range transport of RabA2b-containing vesicles. In Δ*ARKabc,* the number of long-distance movements of mNG-RabA2b slightly decreased, whereas ectopic expression of ARKb-mNG restored motility (Fig. 3D). Consistent with these observations, the RabA2b signal at the apex was smaller in Δ*ARKabc* than the control line (Fig. 3A, B). These results suggest that ARK is involved in the microtubule plus-end-directed transport of RabA2b-containing vesicles, in addition to giant organelles.

Microtubule polymerisation dynamics are unaltered in the absence of ARK in moss

Arabidopsis ARK1 promotes microtubule catastrophe in root hair cells [29]. To examine whether this holds true for moss ARK in protonemata, we used oblique illumination fluorescence microscopy to trace individual microtubule ends in protonemal apical cells in the mutants [39]. Most of the parameters of microtubule dynamics, including catastrophe frequency, were not significantly altered in Δ*ARKabc* or Δ*ARKabcd* (Fig. S2A, Table S1). The growth rate was slightly increased in Δ*ARKabc* but not in Δ*ARKabcd*. Microtubule orientation near the cell tip was further analysed through tracing EB1-Citrine, which binds to the growing ends of microtubules. Similarly, drastic difference was not detected between Δ*ARKabc* and control (Fig. S2B). Thus, the observed phenotype of the mutants is unlikely to be due to the misregulation of polymerisation dynamics or the misorientation of the microtubules.

ARK shows processive, plus-end-directed motility *in vivo*

227 Although endogenous ARKs labelled with Citrine were localised to the microtubules,
228 directional movement was not detected in a previous study [27]. However, the observed lack
229 of motility might have been due to the insufficient sensitivity of the microscopy, which
230 could not detect a single Citrine molecule [40]. In the present study, the brighter fluorescent
231 protein mNG [41] was used to label endogenous ARKb and its localisation was revisited.
232 Consistent with the previous study, ARKb-mNG was observed on microtubules. Most of
233 them were dissociated from microtubules without showing motility (Fig. 4A, C, Movie
234 2). Interestingly, however, some small punctate signals moved along the microtubules at
235 572 ± 243 nm/s (velocity, ±SD) for 986 ± 416 nm (run length, ±SD) (Fig. 4B–D). These
236 values are comparable to those of retrograde transporters (kinesin-14s) in moss (KCBPb,
237 ~413 nm/s, ~1.0 µm: KCHa, ~441 nm/s, ~1.6 µm) [21,28] but much faster than microtubule
238 growth (<100 nm/s; Fig. S2). In contrast, no movement was observed in the rigor mutant
239 ARKb (T169N) -mNG (Fig. 4C). These results suggest that moss ARK is capable of
240 transporting cargo *in vivo*.
241
242 **Tail region of ARK is required for organelle distribution and protonemal growth**
243 ARK family kinesins are distinguished from other kinesins by the presence of an
244 armadillo (ARM) repeat in the tail region, which is known as a protein-protein interaction
245 motif [42]. The ARM domain in the tail region is dispensable for AtARK1 to regulate
246 microtubule catastrophe [43]. However, if ARK is a cargo transporter, the tail would be a
247 potential cargo-binding site, and therefore, critical for its function. To test whether ARM
248 is required for ARK functions, two deletion constructs were transformed into Δ*ARKabc*
249 (Fig. S3A). Interestingly, the constructs lacking ARM (ΔARM, ΔTail) failed to rescue
250 protonemal tissue growth or the position of the chloroplasts (Fig. S3B, C). Thus, not only
251 motor activity, but also ARM, is indispensable for ARK function in moss.
252
253 **ARK enables polarised cell growth by localising RopGEF to the cell tip**
254 A prominent phenotype associated with *ARK* deletion is the suppression of
255 protonemal tissue growth (Fig. 1). At the cellular level, we observed that the protonemal
256 apical and subapical cells were shorter in the mutants than the control line (Fig. 5A, B).
257 One possible explanation for this phenotype is the shortening of the cell cycle (i.e.
258 precocious entry into the M-phase) [44]. However, this was not the case, because the
259 duration of the cell cycle was unchanged between the two rounds of mitosis in Δ*ARKabc*
260 (Fig. S4A). Instead, tip elongation significantly slowed in Δ*ARKabc*, which was
261 consistent with the prevalence of shorter cells (Fig. 5C). Furthermore, protonemal cells
262 in Δ*ARKabcd* exhibited round morphology, suggesting that cell polarity was disturbed
263 (Fig. 5A, right). To analyse this phenotype in more detail, we introduced an inducible
264 RNAi construct targeting *ARKd* into Δ*ARKabc* and observed tip growth upon RNAi
265 induction. Unlike the Δ*ARKabcd* cells, the protonemal cells of this line were rod-shaped
266 before RNAi induction, such that the requirement of ARK for polarised growth could be
267 directly assessed by time-lapse imaging after RNAi induction. We observed that the
268 protonemal cells frequently produced multiple tips in the RNAi line (Fig. S5A, B).
269 The slowing or suppression of tip growth in protonemal cells is reminiscent of the
270 results of actin dysfunction (confirmed in Fig. S4B) [45,46]. Indeed, F-actin foci at the cell
271 apex, which ensure rapid tip growth (Wu and Bezanilla, 2018), were less frequently
272 observed in the absence of *ARKabc* (Fig. 5D, E). We investigated whether the actin

phenotype could be explained within the framework of microtubule-based transport driven by ARK. In animals, proper actin organisation and dynamics for cell motility require the activation of Rho family small GTPases (called ROP in plants), which then activate the actin polymerisation factor formin [47–49]. The cortical localisation of function-verified Rop4-mNG [50] was unchanged in the Δ*ARKabc* mutant (Fig. S4C, D). Interestingly, however, in Δ*ARKabc* we observed a reduction in the cortical signals from RopGEF3 and RopGEF6, the guanine nucleotide exchange factor (GEF) of ROP, and For2A, a class II formin that is required for rapid actin elongation and formation of actin filaments during cell tip growth in moss [51] (Fig. 6A–D). Consistent with these reductions, oblique illumination microscopy revealed that the growth rate of actin filament near the tip was reduced by 14% compared to that in the control line (Fig. 5F). Other Rop-GEFs tagged with mNG were either undetectable or very weakly expressed; therefore, they were not studied further. The necessity of microtubules for apical enrichment of RopGEF3 and RopGEF6 was confirmed by oryzalin treatment followed by time-lapse microscopy (Fig. S4E, F).

We reasoned that if the tip growth defect in the *ARK* mutant could be attributed to a defect in the apical transport of actin regulatory molecules, the ectopic expression and forced apical localisation of RopGEFs would restore the tip growth of the *ΔARKabc* mutant. To test this hypothesis, we ectopically expressed RopGEF3-mNG in Δ*ARKabc*. Colony growth slightly recovered in the transgenic line (Fig. 6H). Next, we constructed a fusion gene in which tail-deleted ARKb was fused to RopGEF3-mNG and expressed it in Δ*ARKabc* (Fig. 6E). As expected from a protein with the plus-end-directed motility, the fusion protein was enriched at the apical cell tip (Fig. 6F, bottom). However, because the ARM domain was absent in this construct, the chloroplast distribution was not restored (Fig. 6G). However, the fusion construct substantially restored colony growth (Fig. 6F, H). Thus, the forced delivery of RopGEF3 to the cell tip using an anterograde motor was sufficient to restore cell tip growth.

Partial complementation of Pp*ARK* mutant by AtARKs

Finally, to gain insight into the evolutionary conservation of ARK function, we examined whether ectopic expression of *A. thaliana* ARK could rescue the moss *ARK* mutant phenotypes. To this end, we attempted to express AtARK1, AtARK2, and AtARK3 in moss Δ*ARKabc*. For unknown reasons, transformants expressing AtARK1 could not be obtained, despite multiple attempts. However, lines stably expressing AtARK2-mNG or AtARk3-mNG were successfully generated. The moss expressing AtARK2 or AtARK3 grew slightly faster than the parental Δ*ARKabc* line, and the colony on the plate showed protonemal tissue more clearly (Fig. 7A, top). Robust growth of the protonemal filament was also observed in the images of a 6-day-old protonema regenerated from a single protoplast (Fig. 7A, bottom). Thus, AtARK2 and AtARK3 partially rescued this growth phenotype. In contrast, AtARK did not rescue the nuclear position (Fig. 7B, arrowheads). The basal accumulation of chloroplasts in Δ*ARKabc* disappeared after ectopic expression of AtARK2 but not that of AtARK3 (Fig. 7B, C). Interestingly, AtARK2 expression resulted in an apical shift of the chloroplast, which is somewhat reminiscent of the *KCBP* knockout line [22]. Thus, we conclude that AtARK2 and AtARK3 can substitute for a subset of moss ARK functions.

Discussion

ARK is a versatile anterograde transporter in plants

A long sought-after in plant microtubule biology is an anterograde transporter that can carry a variety of cargos [3,52–54]. Several data presented in this study suggest that it could be ARK, which is a widely conserved kinesin in plants.

First, the movement of three giant organelles and RabA2-marked vesicles was suppressed in the *ARKabc* triple mutant. Because movement towards the apex was suppressed and microtubule polarity was unchanged in the mutant, we concluded that ARK is responsible for the plus-end-directed motility of these organelles. Using Δ*ARKabcd*, we also demonstrated that microtubule polymerisation dynamics were unperturbed in the absence of ARK. Thus, an alternative microtubule-based mechanism, namely, microtubule polymerisation-based pushing [31,55], is unlikely to be the cause of abnormal motility. The most natural interpretation is that ARK transports cargo to the microtubule plus-end. We speculate that the residual apical motility observed in the Δ*ARKabc* mutant is driven by the intact ARKd protein. However, the possibility that additional motor families also play a role in the transport of these cargo cannot be ruled out. For example, in *Arabidopsis*, vesicular transport on cortical microtubules requires the FRA1 protein, which is a processive, plus-end-directed kinesin belonging to the kinesin-4 family [56–58].

Second, we detected the processive motility of ARKb proteins *in vivo*. The velocity and run length were comparable to those of retrograde motors (KCBP and KCH), supporting the idea that the tug-of-war between ARK and the retrograde motors underlies bidirectional transport of cargos. However, it remains unclear whether the motile ARKb-mNG signals represent cargo-carrying or cargo-free ARKb proteins. Because a significant population of ARK proteins are bound to microtubules but are not motile, an intriguing possibility is that cargo binding activates the motor and initiates motility. In contrast to wild-type ARKb, the rigor mutant did not show motility or rescue the mutant phenotype, which is consistent with the notion that ARKb acts as a transporter.

Third, the ARM domain in the tail region is critical for nuclear and chloroplast motility. The tail domain is essential for the function of cargo-carrying kinesins, because it is generally the binding site for cargo. In contrast, the tail of kinesin-13 or AtARK1 is dispensable for the regulation of microtubule dynamics [43,59]. The criticality of ARM is consistent with the model in that it serves as the cargo-binding site.

Fourth, the mutant phenotype is pleotropic. Our cellular analysis was conducted only in protonemal tissues, which are excellent for analysing microtubule-based transport. However, ARK plays an important role in rhizoids and gametophores, and their development is abnormal in Δ*ARKabcd*. Determining which specific cellular defect is attributable to the phenotype is an interesting future research topic.

Finally, AtARK2 and AtARK3 partially restored organelle position and protonemal growth in the *ΔARKabc* mutant of *P. patens*. Thus, the transport function of ARK may be conserved in angiosperms. The *AtARK2* mutant showed helical root growth, indicating that ARK2 is required for the proper growth of root epidermal cells [60]. In contrast, ARK3 is thought to be essential for plant development [61]. Abnormal distribution of stomata was observed upon cell type- and cell cycle-specific ARK3 knockdown in stomatal meristemoid mother cells [62]. These phenotypes might be the consequence of

365 mislocalisation of AtARK cargos. Whether AtARK1 has a similar function remains
366 unclear. Given the phylogenetic distance and the reported cellular activity that has not
367 been observed in moss, it might have differentiated to acquire novel functions. In the
368 accompanying paper, liverwort ARK was shown to be required for organelle movement,
369 further illustrating the evolutionary conservation of ARK as a transporter (Kanda et al.
370 co-submitted).
371 Taken together, ARK is the strongest candidate for a universal anterograde
372 transporter in plants, which carries a variety of cargos, including nuclei, chloroplasts,
373 mitochondria, and vesicles, towards the microtubule plus ends (Fig. 7D).
374
375 **Microtubule-dependent transport supports tip growth**
376 Tip growth is a growth form found in several plant cell types, such as pollen tubes,
377 root hairs, and moss protonemata [63], as well as in many other systems, including
378 macroalgae, fungi, and neural axons in animals [64–66]. Regulated plasticisation of the cell
379 wall and vesicular transport of membrane and cell wall materials are important factors in
380 the tip growth of walled organisms [65,67]. Regarding the cytoskeleton, the primary player
381 in tip growth is actin. For example, in *P. patens* protonemata, the addition of actin
382 inhibitors immediately and completely stops tip growth [45]. In contrast, microtubules are
383 thought to play a role in determining growth orientation. Cell tip expansion and abnormal
384 outgrowth in non-apical regions have been reported after the addition of microtubule-
385 depolymerising drugs [45]. However, the detailed mechanism by which microtubules define
386 growth direction remains elusive.
387 Our analyses suggest that the microtubule- and ARK-dependent transport of actin
388 regulatory molecules is critical for polarised tip growth. First, the rigor mutant of ARK
389 could not restore tip growth. Second, actin regulatory molecules (RopGEF3, RopGEF6,
390 and formin) and F-actin itself were less enriched at the apex in the *ARK* mutant. Third,
391 and most notably, the growth phenotype was partially rescued by the artificial delivery of
392 RopGEF3 to the apex by tailless ARKb. This result suggests that in wild-type moss,
393 RopGEF or the upstream factor required for RopGEF localisation is transported by ARK.
394 However, only a partial rescue of the phenotype by RopGEF force-localisation suggests
395 that ARK transports other molecules critical for tip growth in addition to actin regulators.
396 Identification of the cargo molecules would further clarify the versatility of ARK as a
397 transporter and the detailed molecular mechanism of ARK-dependent tip growth.
398 Conceptually, the mechanism by which ARK-dependent anterograde transport
399 regulates polarised cell growth is remarkably similar to what has been revealed in the
400 fission yeast *Schizosacharomyces pombe*, an organism with one of the best-studied cell
401 growth systems [68]. In fission yeast, bipolar cell growth during interphase is ensured by
402 bipolar microtubule networks and the plus-end and cortical accumulation of the Tea1-
403 Tea4 complex, which recruits formin For3 [69,70]. The molecule important for Tea1-Tea4
404 localisation is the processive, plus-end-directed kinesin Tea2 [71–73]. In the absence of Tea2,
405 cells that initiate growth from improper sites are observed, which is likely driven by actin
406 that is not restricted to a single site [71]. An analogous mechanism is found in the
407 filamentous fungus *Aspergillus nidulans* [65]. Interestingly, the transport of polarity factors
408 by anterograde motors is critical for cell morphogenesis also in mammalian cells. In
409 epithelial cells, microtubules form uniform arrays along the apico-basolateral polarity
410 axis, and several anterograde kinesins have been suggested to transport key polarity

411 proteins associated with epithelial morphogenesis [74–76]. Thus, long-distance transport of
412 polarisation factors along microtubules might be a general scheme for polarised growth
413 in a wide range of eukaryotic cells.
414

415 Materials and methods

416

417 *P. patens* culture and transformation

418 All strains in this study were derived from the Gransden ecotype of *Physcomitrium*
419 (*Physcomitrella*) *patens* [77]. *P. patens* culture and transformation protocols followed were
420 as described by Yamada et al. (2016). Briefly, mosses were regularly cultured on BCDAT
421 plates at 25 °C under continuous light illumination. A standard polyethylene glycol
422 (PEG)-mediated method was exploited for transformation. Prior to transformation,
423 sonicated protonemata were cultured on BCDAT agar medium for 5–6 days. Transgenic
424 lines were selected using corresponding antibiotics. Line confirmation was conducted
425 through genotyping PCR and visual inspection. Sequencing was performed to confirm
426 the CRISPR mutant lines. The lines generated in this study are listed in Table S2.
427

428 Plasmid construction

429 The plasmids and primers used in this study are listed in Tables S3 and S4, respectively.
430 CRISPR targets with high specificity were manually selected around the ATPase motif
431 (P-loop) or microtubule binding site (called the Switch 2 region) in the motor domain of
432 *ARK* genes. All target sequences were synthesised and ligated into the *Bsa*I site of
433 pPY156, which is based on pCasGuide/pUC18 and contains a hygromycin-resistant
434 cassette [78]. For endogenous tagging via homologous recombination, the plasmid was
435 constructed using the In-Fusion HD Cloning Kit (Takara); 1–2 kb sequences of the 5′ and
436 3′ ends of the genes of interest flanked the fragment that consisted of an in-frame linker,
437 mNeonGreen (mNG) coding sequence, Flag tag, and G418 resistant cassette. The mNG
438 codon was optimised for expression in *Arabidopsis* [33]. To generate the Rop4-mNG
439 plasmid, the fusion constructs were constructed as described by Cheng et al. (2020). For
440 the rescue experiment, the *ARKb* coding sequence was amplified from the moss cDNA
441 library and ligated into the pENTR/D-TOPO vector containing the in-frame linker, mNG-
442 coding sequence, and Flag tag, followed by the Gateway LR reaction (Invitrogen) into
443 the pPY138 vector containing the *EF1α* promoter, G418 resistance cassette, and 1-kb
444 sequences homologous to the *hb7* locus. Likewise, the gene sequences of *A. thaliana*
445 *ARK2* and *ARK3* were amplified from a cDNA library (a gift from Dr Hidefumi Shinohara
446 [Fukui Prefectural University]) and cloned into an overexpression vector containing the
447 *EF1α* promoter.
448

449 Moss colony assay

450 To prepare the protoplasts, 5–7-day-old sonicated protonemata were digested with an 8%
451 (w/v) mannitol solution supplemented with 1% (w/v) driselase for 0.5–1 h. After
452 removing the driselase by washing twice with 8% mannitol solution, the protoplasts were
453 resuspended in the protoplast regeneration liquid [46,79]. After 4 h of incubation in the dark,
454 the protoplasts were collected by centrifugation, resuspended in 7.5 mL of protoplast

455 regeneration media (PRM) solution [79], and spread onto three PRM plates covered with
456 cellophane. The protoplasts were cultured for 3 days and transferred to a BCDAT plate.
457 Images of 7-day-old moss protonemata were taken using a stereomicroscope SMZ800N
458 (Nikon) equipped with an ILCE-QX1 camera (SONY). Nine-day-old protonemata were
459 inoculated onto BCDAT plates and cultured for 3–5 weeks. Images of overall colonies or
460 gametophores were captured using a C-765 Ultra Zoom digital camera (Olympus) or
461 SMZ800N, respectively.
462

463 **Microscopy**

464 Time-lapse microscopy was performed as described by Nakaoka et al. (2012). Briefly, in
465 the long-term time-lapse imaging experiments for the observation of protonemal cells,
466 the protonemata were cultured on thin layers of BCD agarose in 6-well glass-bottom
467 dishes for 5–7 days. Epifluorescence images were acquired with a Nikon Ti microscope
468 (10× 0.45 NA lens, Zyla 4.2P CMOS camera (Andor), Nikon Intensilight Epi-
469 fluorescence Illuminator) at intervals of 3–30 min with white light between acquisitions.
470 For high-resolution imaging, protonemata were inoculated onto the agar pad in a 35 mm
471 glass-bottom dish, followed by culturing for 5–7 days. Confocal imaging was performed
472 with a Nikon Ti microscope attached to a CSU-X1 spinning disk confocal scanner unit
473 (Yokogawa), EMCCD camera (ImagEM, Hamamatsu), and three laser lines (637, 561,
474 and 488 nm). Lenses were selected depending on the experiment (40× 1.30 NA, 60× 1.40
475 NA, and 100× 1.45 NA). Oblique illumination fluorescence microscopy was performed
476 using a Nikon Ti microscope attached to a total internal reflection fluorescence (TIRF)
477 unit, 100× 1.49-NA lens, GEMINI split view (Hamamatsu), and EMCCD camera Evolve
478 (Roper) [40]. The samples for oblique imaging were prepared with a microfluidic device of
479 15 μm height . Stock solutions of oryzalin, latrunculin A, and FM4-64 in DMSO were
480 diluted with distilled water to working concentrations of 10 μM oryzalin, 25 μM
481 latrunculin A, and 10 μM FM4-64. Prior to drug addition, the protonemal tissue on the
482 agarose pad was preincubated in water for 1 h for absorption. After water removal, 1 mL
483 of the drug solution was added, and image acquisition was started immediately. DMSO
484 was used as a control. To induce RNAi, 1 μM β-estradiol was added to the 4–5-day-old
485 protonemata on sample dishes 12 h prior to observation. Most of the imaging was
486 performed at 22–25 °C in the dark, except for the images shown in Figure S5A, which
487 were taken under continuous light.
488

489 **Image data analysis**

490 All raw data processing and measurements were performed using the Fiji software.
491

492 *Moss colony size.* The moss colony images were outlined automatically, and the area was
493 measured using Fiji.
494

495 *Velocity and run length of ARKb.* Oblique illumination time-lapse images of the
496 endoplasmic microtubules in protonemal cells were taken every 200 ms. The
497 microtubules on which single or multiple ARKb-mNeonGreen particles were
498 continuously moving were manually selected and analysed. A kymograph was generated

along the microtubule, and the inclination and distance of the line derived from ARKb particles were measured as the velocity and run length, respectively.

Microtubule plus-end dynamics and orientation. To quantify the plus end growth/shrinkage rate and rescue/catastrophe frequency, we followed the protocol described by Leong et al. (2020). Briefly, oblique illumination time-lapse images of endoplasmic microtubules in protonemal cells were taken every 3 s for 3 min. Then, a 5 × 6 μm area was randomly selected in each cell, and kymographs of every traceable microtubule plus end in the area were created. The inclination of the microtubules in the kymographs, which corresponded to the growth or shrinkage rate, was measured. To determine catastrophe or rescue frequency, the number of events was counted and divided by the observed growth or shrinkage duration of the microtubule, respectively. The growth rate at the cell apex was specifically determined using EB1-Citrine imaging, which tracks growing plus ends. Time-lapse images of EB1-Citrine were acquired every 3 s using a spinning-disc confocal microscope. Kymographs were generated along the edge of the caulonemal cell apex. The inclination of EB1-Citrine signals was measured to determine the microtubule growth rate. To analyse microtubule orientation in interphase apical cells, cells were observed for > 150 min after anaphase onset. Kymographs were generated along the edges of the cells, and the directionality of EB1-Citrine comets was measured to determine the overall orientation of the microtubules [81].

Actin growth rate. Time-lapse images of apical cell tips of the Lifeact-mNG expressing line were taken every 200 ms using TIRF microscopy. The elongating Lifeact-mNG at the cell tip was tracked and used to generate kymographs. The inclination of the Lifeact-mNG on the kymograph was measured as the growth rate of the actin filament. We noted that actin dynamics parameters were sensitive to the expression levels of Lifeact-mNG. Therefore, we used the same parental line expressing Lifeact-mNG in this experiment and analysis.

Spindle position and cell length. For apical cells, time-lapse images were obtained every 3 min, and the distance between the basal cell wall and cell tip (i.e. cell length) or the spindle equator was measured just before anaphase onset. The relative position of the metaphase spindle was determined using division. The length of the subapical cells was measured based on a snapshot of caulonemal filaments.

Subapical cell length. Images of moss protonemata stained with FM4-64 were obtained. The lengths of the subapical cells of the caulonemal filaments were measured.

Cell cycle duration. Time-lapse images of the caulonemal cells were obtained every 10 min. The duration between the nuclear envelope breakdown (NEBD) of the mother cell and the NEBD of the daughter apical cell was measured.

Nuclear movement. Time-lapse images were taken every 3 min. The distance between the cell plate and centre of the nucleus was measured in apical cells before and after cell

division. Similarly, the distance between the apical cell wall and the centre of the nucleus was measured in subapical cells with a bulge.

Chloroplast distribution. Time-lapse images were taken every 3 min. The intensity of chloroplast autofluorescence along the long axis of caulonemal apical cells was measured 150 min after anaphase onset, and the background intensity of each image was subtracted. The intensity of each pixel on the drawn line was divided by the mean intensity of the entire length of the line to get relative intensity. The cells were divided into ten sections, and the average relative intensity of each section is displayed.

Mitochondrial movement. To visualise mitochondria, γ-F1ATPase-mNG was expressed under the *EF1α* promotor [82]. A kymograph was created from images acquired every 2 s using oblique illumination fluorescence microscopy. To quantify mitochondrial relocation, time-lapse images of the apical side of caulonemal apical cells were obtained every 10 s for 6 min using spinning-disc confocal microscopy. The majority of the microtubules in this area are oriented in such a manner that the plus ends face the apex [20], enabling a reliable estimate of whether mitochondria tend to move towards the plus or minus end. In this analysis, 15 μm^2 was selected in the area between the cell apex and nucleus, and six mitochondria that were clearly identified were analysed. The position of each mitochondrion in the first and last frame was compared; based on the overall microtubule polarity, translocation towards the tip was interpreted as anterograde motility.

Intensity of mNG-RabA2b and For2A-mNG. The apex of caulonemal cells in which mNG-RabA2b or For2A-mNG was expressed was imaged using a z-series taken every 0.5 µm for a range of 15 µm. The sums of the slices were made by z-projection using the Fiji software. The mean intensity within approximately 2 μm^2 of the punctate signals was measured and subtracted by the background intensity.

Movement of mNG-RabA2b puncta. Images of caulonemal apical cells expressing mNG-RabA2b were taken every 200 ms using a spinning-disc confocal microscope. The number of signal puncta moving >10 µm in a minute was counted for each cell.

Tip growth rate. Time-lapse epifluorescent images of protonemata were obtained every 3 min using a 10× lens. Kymographs were created along the axes of growing caulonemal filaments, and the slope of the kymographs was measured to obtain the growth rate.

Cell morphology observation under ARKd RNAi. The moss protonemata were cultured on BCDAT for 4–5 days, and 1 µM β-estradiol or the control (0.1% DMSO) was added to the plant. After four days of incubation following drug addition, the morphology of the apical cells was observed and counted.

Frequency of actin foci formation at the cell apex. The apexes of the cells expressing Lifeact-mNG was imaged using a z-series taken every 0.5 µm for a range of 8 µm for 10 min at 30 s intervals. Following the method described by Yamada and Goshima, (2018), the z-stack images were processed by maximum z-projection with Fiji, and the number of time frames in which the actin focus was clearly observed was counted. The ratio of time frames with clear foci was used to determine the frequency of foci formation.

Intensity of Rop4-mNG and RopGEFs-mNG. The protonemal cell apex of the cell line expressing Rop4-mNG or RopGEFs-mNG was imaged using a z-series taken every 0.5 µm for a range of 15 µm. A slice showing the centre of the cell was selected. The total intensity of mNG signals was measured along the cell edge by drawing a line (width = 0.4 µm) (subtracted by the cytoplasmic background intensity). ROP-GEF6 was distributed more broadly than ROP-GEF3. For the analysis of the temporal change of the intensity under the drug treatment, time-lapse images were acquired every 1 or 3 min using a z-series taken every 1.5 µm for a range of 6 µm. The images were quantified in an identical manner.

Statistical analysis

Welch's two-tailed t-test was used when the samples to be compared comprised two groups. Tukey's multiple comparison test was used to analyse datasets that included more than two groups. All statistical analyses were performed using the R software. The data distribution was assumed to be normal, but this was not formally tested. Obtained P values are denoted as follows: *, $P < 0.05$; **, $P < 0.01$; ***, $P < 0.001$; and ****, $P < 0.0001$. Data from multiple experiments were combined because of insufficient sample numbers in a single experiment, unless otherwise stated.

Accession numbers

The gene sequences used in this study are available in Phytozome under the following accession numbers: *AtARK1* (AT3G54870.3), *AtARK2* (AT1G01950.3), *AtARK3* (AT1G12430.1), *PpARKa* (Pp3c27_850V3.1), *PpARKb* (Pp3c16_2830V3.1), *PpARKc* (Pp3c6_19520V3.1), *PpARKd* (Pp3c2_28160V3.1), and *MpARK* (Mapoly0114s0009.1).

Acknowledgements

We are grateful to Magdalena Bezanilla, Peishan Yi, and Moé Yamada for providing the moss lines and plasmids; Chiemi Koketsu and Rie Inaba for media preparation; and Hiroyasu Motose for communicating unpublished data. This work was funded by the Japan Society for the Promotion of Science KAKENHI (17H06471, 18KK0202, 22H04717, and 22H02644 to GG). MWY is a recipient of the Japan Society for the Promotion of Science pre-doctoral fellowship. The authors declare that they have no conflicts of interest.

References

1. Hirokawa, N. & Noda, Y. Intracellular Transport and Kinesin Superfamily Proteins, KIFs: Structure, Function, and Dynamics. *Physiological Reviews* **88**, 1089–1118 (2008).
2. Reck-Peterson, S. L., Redwine, W. B., Vale, R. D. & Carter, A. P. The cytoplasmic dynein transport machinery and its many cargoes. *Nat Rev Mol Cell Biol* **19**, 382–398 (2018).
3. Vale, R. D. The Molecular Motor Toolbox for Intracellular Transport. *Cell* **112**, 467–480 (2003).
4. Encalada, S. E. & Goldstein, L. S. B. Biophysical Challenges to Axonal Transport: Motor-Cargo Deficiencies and Neurodegeneration. *Annual Review of Biophysics* **43**, 141–169 (2014).
5. Hirokawa, N., Niwa, S. & Tanaka, Y. Molecular Motors in Neurons: Transport Mechanisms and Roles in Brain Function, Development, and Disease. *Neuron* **68**, 610–638 (2010).
6. Vale, R. D., Reese, T. S. & Sheetz, M. P. Identification of a novel force-generating protein, kinesin, involved in microtubule-based motility. *Cell* **42**, 39–50 (1985).
7. Leopold, P. L., McDowall, A. W., Pfister, K. K., Bloom, G. S. & Brady, S. T. Association of kinesin with characterized membrane-bounded organelles. *Cell Motility* **23**, 19–33 (1992).
8. Nakata, T. & Hirokawa, N. Microtubules provide directional cues for polarized axonal transport through interaction with kinesin motor head. *The Journal of cell biology* **162**, 1045–1055 (2003).
9. Splinter, D. *et al.* Bicaudal D2, Dynein, and Kinesin-1 Associate with Nuclear Pore Complexes and Regulate Centrosome and Nuclear Positioning during Mitotic Entry. *PLOS Biology* **8**, e1000350 (2010).
10. Tanaka, Y. *et al.* Targeted Disruption of Mouse Conventional Kinesin Heavy Chain kif5B, Results in Abnormal Perinuclear Clustering of Mitochondria. *Cell* **93**, 1147–1158 (1998).
11. Zimyanin, V. L. *et al.* In Vivo Imaging of oskar mRNA Transport Reveals the Mechanism of Posterior Localization. *Cell* **134**, 843–853 (2008).
12. Rogers, S. L. & Gelfand, V. I. Membrane trafficking, organelle transport, and the cytoskeleton. *Current Opinion in Cell Biology* **12**, 57–62 (2000).
13. Welte, M. A. Bidirectional Transport along Microtubules. *Current Biology* **14**, R525–R537 (2004).
14. Shimmen, T. & Yokota, E. Cytoplasmic streaming in plants. *Current Opinion in Cell Biology* **16**, 68–72 (2004).
15. Tominaga, M. & Ito, K. The molecular mechanism and physiological role of cytoplasmic streaming. *Current Opinion in Plant Biology* **27**, 104–110 (2015).
16. Tamura, K. *et al.* Myosin XI-i Links the Nuclear Membrane to the Cytoskeleton to Control Nuclear Movement and Shape in Arabidopsis. *Current Biology* **23**, 1776–1781 (2013).
17. Kong, S.-G. & Wada, M. Molecular basis of chloroplast photorelocation movement. *Journal of plant research* **129**, 159–166 (2016).
18. Muroyama, A., Gong, Y. & Bergmann, D. C. Opposing, Polarity-Driven

676 Nuclear Migrations Underpin Asymmetric Divisions to Pattern Arabidopsis Stomata.
677 *Current Biology* **30**, 4467-4475.e4 (2020).
678 19. Zonia, L., Tupý, J. & Staiger, C. J. Unique actin and microtubule arrays co-
679 ordinate the differentiation of microspores to mature pollen in Nicotiana tabacum.
680 *Journal of Experimental Botany* **50**, 581–594 (1999).
681 20. Hiwatashi, Y., Sato, Y. & Doonan, J. H. Kinesins Have a Dual Function in
682 Organizing Microtubules during Both Tip Growth and Cytokinesis in Physcomitrella
683 patens. *The Plant Cell* **26**, 1256–1266 (2014).
684 21. Yamada, M. & Goshima, G. The KCH Kinesin Drives Nuclear Transport and
685 Cytoskeletal Coalescence to Promote Tip Cell Growth in Physcomitrella patens. *The*
686 *Plant Cell* **30**, 1496–1510 (2018).
687 22. Yamada, M., Tanaka-Takiguchi, Y., Hayashi, M., Nishina, M. & Goshima, G.
688 Multiple kinesin-14 family members drive microtubule minus end–directed transport in
689 plant cells. *Journal of Cell Biology* **216**, 1705–1714 (2017).
690 23. Yoshida, M. W., Yamada, M. & Goshima, G. Moss Kinesin-14 KCBP
691 Accelerates Chromatid Motility in Anaphase. *Cell Structure and Function* **44**, 95–104
692 (2019).
693 24. Shen, Z., Collatos, A. R., Bibeau, J. P., Furt, F. & Vidali, L. Phylogenetic
694 Analysis of the Kinesin Superfamily from Physcomitrella. *Front. Plant Sci.* **3**, (2012).
695 25. Gabrych, D. R., Lau, V. Z., Niwa, S. & Silverman, M. A. Going Too Far Is the
696 Same as Falling Short†: Kinesin-3 Family Members in Hereditary Spastic Paraplegia.
697 *Frontiers in Cellular Neuroscience* **13**, (2019).
698 26. Siddiqui, N. & Straube, A. Intracellular cargo transport by kinesin-3 motors.
699 *Biochemistry Moscow* **82**, 803–815 (2017).
700 27. Miki, T., Nishina, M. & Goshima, G. RNAi Screening Identifies the Armadillo
701 Repeat-Containing Kinesins Responsible for Microtubule-Dependent Nuclear
702 Positioning in Physcomitrella patens. *Plant and Cell Physiology* **56**, 737–749 (2015).
703 28. Jonsson, E., Yamada, M., Vale, R. D. & Goshima, G. Clustering of a kinesin-
704 14 motor enables processive retrograde microtubule-based transport in plants. *Nature*
705 *Plants* **1**, 1–7 (2015).
706 29. Eng, R. C. & Wasteneys, G. O. The microtubule plus-end tracking protein
707 ARMADILLO-REPEAT KINESIN1 promotes microtubule catastrophe in Arabidopsis.
708 *Plant Cell* **26**, 3372–3386 (2014).
709 30. Sun, J., Zhang, M., Qi, X., Doyle, C. & Zheng, H. Armadillo-repeat kinesin1
710 interacts with Arabidopsis atlastin RHD3 to move ER with plus-end of microtubules.
711 *Nat Commun* **11**, 5510 (2020).
712 31. Tran, P. T., Marsh, L., Doye, V., Inoué, S. & Chang, F. A Mechanism for
713 Nuclear Positioning in Fission Yeast Based on Microtubule Pushing. *Journal of Cell*
714 *Biology* **153**, 397–412 (2001).
715 32. Lopez-Obando, M. *et al.* Simple and efficient targeting of multiple genes
716 through CRISPR-Cas9 in Physcomitrella patens. *G3: Genes, Genomes, Genetics* **6**,
717 3647–3653 (2016).
718 33. Yi, P. & Goshima, G. Transient cotransformation of CRISPR/Cas9 and
719 oligonucleotide templates enables efficient editing of target loci in Physcomitrella
720 patens. *Plant Biotechnology Journal* **18**, 599–601 (2020).
721 34. Kull, F. J., Sablin, E. P., Lau, R., Fletterick, R. J. & Vale, R. D. Crystal
722 structure of the kinesin motor domain reveals a structural similarity to myosin. *Nature*

723 **380**, 550–555 (1996).
724 35. Nakata, T. & Hirokawa, N. Point mutation of adenosine triphosphate-binding
725 motif generated rigor kinesin that selectively blocks anterograde lysosome membrane
726 transport. *Journal of Cell Biology* **131**, 1039–1053 (1995).
727 36. Orr, R. G., Cheng, X., Vidali, L. & Bezanilla, M. Orchestrating cell
728 morphology from the inside out – using polarized cell expansion in plants as a model.
729 *Current Opinion in Cell Biology* **62**, 46–53 (2020).
730 37. Chow, C.-M., Neto, H., Foucart, C. & Moore, I. Rab-A2 and Rab-A3 GTPases
731 define a trans-golgi endosomal membrane domain in Arabidopsis that contributes
732 substantially to the cell plate. *Plant Cell* **20**, 101–123 (2008).
733 38. Pang, L. *et al.* The small GTPase RABA2a recruits SNARE proteins to
734 regulate the secretory pathway in parallel with the exocyst complex in Arabidopsis.
735 *Molecular Plant* **0**, (2021).
736 39. Leong, S. Y., Edzuka, T., Goshima, G. & Yamada, M. Kinesin-13 and Kinesin-
737 8 Function during Cell Growth and Division in the Moss Physcomitrella patens. *The*
738 *Plant Cell* **32**, 683–702 (2020).
739 40. Nakaoka, Y., Kimura, A., Tani, T. & Goshima, G. Cytoplasmic nucleation and
740 atypical branching nucleation generate endoplasmic microtubules in Physcomitrella
741 patens. *The Plant Cell* **27**, 228–242 (2015).
742 41. Shaner, N. C. *et al.* A bright monomeric green fluorescent protein derived from
743 Branchiostoma lanceolatum. *Nat Methods* **10**, 407–409 (2013).
744 42. Coates, J. C. Armadillo repeat proteins: beyond the animal kingdom. *Trends in*
745 *Cell Biology* **13**, 463–471 (2003).
746 43. Eng, R. C. *et al.* The ARM Domain of ARMADILLO-REPEAT KINESIN 1 is
747 Not Required for Microtubule Catastrophe But Can Negatively Regulate NIMA-
748 RELATED KINASE 6 in Arabidopsis thaliana. *Plant and Cell Physiology* **58**, 1350–
749 1363 (2017).
750 44. Russell, P. & Nurse, P. Negative regulation of mitosis by wee1+, a gene
751 encoding a protein kinase homolog. *Cell* **49**, 559–567 (1987).
752 45. Doonan, J. H., Cove, D. J. & Lloyd, C. W. Microtubules and microfilaments in
753 tip growth: evidence that microtubules impose polarity on protonemal growth in
754 Physcomitrella patens. *Journal of Cell Science* **89**, 533–540 (1988).
755 46. Vidali, L., Augustine, R. C., Kleinman, K. P. & Bezanilla, M. Profilin is
756 essential for tip growth in the moss Physcomitrella patens. *The Plant Cell* **19**, 3705–
757 3722 (2007).
758 47. Burkart, G. M., Baskin, T. I. & Bezanilla, M. A family of ROP proteins that
759 suppresses actin dynamics, and is essential for polarized growth and cell adhesion. *J*
760 *Cell Sci* **128**, 2553–2564 (2015).
761 48. Etienne-Manneville, S. & Hall, A. Rho GTPases in cell biology. *Nature* **420**,
762 629–635 (2002).
763 49. Kost, B. Spatial control of Rho (Rac-Rop) signaling in tip-growing plant cells.
764 *Trends in Cell Biology* **18**, 119–127 (2008).
765 50. Cheng, X., Mwaura, B. W., Chang Stauffer, S. R. & Bezanilla, M. A fully
766 functional ROP fluorescent fusion protein reveals roles for this GTPase in subcellular
767 and tissue-level patterning. *Plant Cell* **32**, 3436–3451 (2020).
768 51. Vidali, L. *et al.* Rapid formin-mediated actin-filament elongation is essential
769 for polarized plant cell growth. *Proceedings of the National Academy of Sciences* **106**,

770 13341–13346 (2009).
771 52. Asada, T. & Collings, D. Molecular motors in higher plants. *Trends in Plant*
772 *Science* **2**, 29–37 (1997).
773 53. Kaothien, P. *et al.* Kinase partner protein interacts with the LePRK1 and
774 LePRK2 receptor kinases and plays a role in polarized pollen tube growth. *Plant J* **42**,
775 492–503 (2005).
776 54. Reddy, A. S. N. Molecular motors and their functions in plants. in
777 *International Review of Cytology* vol. 204 97–178 (Elsevier, 2001).
778 55. Piel, M. & Tran, P. T. Cell Shape and Cell Division in Fission Yeast. *Current*
779 *Biology* **19**, R823–R827 (2009).
780 56. Kong, Z. *et al.* Kinesin-4 Functions in Vesicular Transport on Cortical
781 Microtubules and Regulates Cell Wall Mechanics during Cell Elongation in Plants.
782 *Molecular Plant* **8**, 1011–1023 (2015).
783 57. Zhu, C. & Dixit, R. Single Molecule Analysis of the Arabidopsis FRA1
784 Kinesin Shows that It Is a Functional Motor Protein with Unusually High Processivity.
785 *Molecular Plant* **4**, 879–885 (2011).
786 58. Zhu, C. *et al.* The fragile Fiber1 kinesin contributes to cortical microtubule-
787 mediated trafficking of cell wall components. *Plant Physiology* **167**, 780–792 (2015).
788 59. Maney, T., Wagenbach, M. & Wordeman, L. Molecular Dissection of the
789 Microtubule Depolymerizing Activity of Mitotic Centromere-associated Kinesin*.
790 *Journal of Biological Chemistry* **276**, 34753–34758 (2001).
791 60. Sakai, T. *et al.* Armadillo repeat-containing kinesins and a NIMA-related
792 kinase are required for epidermal-cell morphogenesis in Arabidopsis. *The Plant Journal*
793 **53**, 157–171 (2008).
794 61. Malcos, J. L. & Cyr, R. J. An ungrouped plant kinesin accumulates at the
795 preprophase band in a cell cycle-dependent manner. *Cytoskeleton* **68**, 247–258 (2011).
796 62. Lau, O. S. *et al.* Direct roles of SPEECHLESS in the specification of stomatal
797 self-renewing cells. *Science* **345**, 1605–1609 (2014).
798 63. Rounds, C. M. & Bezanilla, M. Growth Mechanisms in Tip-Growing Plant
799 Cells. *Annu. Rev. Plant Biol.* **64**, 243–265 (2013).
800 64. Dickson, B. J. Rho GTPases in growth cone guidance. *Current Opinion in*
801 *Neurobiology* **11**, 103–110 (2001).
802 65. Riquelme, M. Tip Growth in Filamentous Fungi: A Road Trip to the Apex.
803 *Annual Review of Microbiology* **67**, 587–609 (2013).
804 66. Shirae-Kurabayashi, M., Edzuka, T., Suzuki, M. & Goshima, G. Cell tip
805 growth underlies injury response of marine macroalgae. *PLOS ONE* **17**, e0264827
806 (2022).
807 67. Bibeau, J. P., Galotto, G., Wu, M., Tüzel, E. & Vidali, L. Quantitative cell
808 biology of tip growth in moss. *Plant Mol Biol* **107**, 227–244 (2021).
809 68. Hachet, O., Bendezú, F. O. & Martin, S. G. Fission yeast: in shape to divide.
810 *Current Opinion in Cell Biology* **24**, 858–864 (2012).
811 69. Martin, S. G., McDonald, W. H., Yates, J. R. & Chang, F. Tea4p Links
812 Microtubule Plus Ends with the Formin For3p in the Establishment of Cell Polarity.
813 *Developmental Cell* **8**, 479–491 (2005).
814 70. Martin, S. G., Rincón, S. A., Basu, R., Pérez, P. & Chang, F. Regulation of the
815 Formin for3p by cdc42p and bud6p. *MBoC* **18**, 4155–4167 (2007).
816 71. Browning, H. *et al.* Tea2p Is a Kinesin-like Protein Required to Generate

Polarized Growth in Fission Yeast. *Journal of Cell Biology* **151**, 15–28 (2000).
72. Browning, H., Hackney, D. D. & Nurse, P. Targeted movement of cell end factors in fission yeast. *Nat Cell Biol* **5**, 812–818 (2003).
73. Busch, K. E., Hayles, J., Nurse, P. & Brunner, D. Tea2p Kinesin Is Involved in Spatial Microtubule Organization by Transporting Tip1p on Microtubules. *Developmental Cell* **6**, 831–843 (2004).
74. Kreitzer, G. & Myat, M. M. Microtubule Motors in Establishment of Epithelial Cell Polarity. *Cold Spring Harb Perspect Biol* **10**, a027896 (2018).
75. Müsch, A. Microtubule Organization and Function in Epithelial Cells. *Traffic* **5**, 1–9 (2004).
76. Rodriguez-Boulan, E. & Macara, I. G. Organization and execution of the epithelial polarity programme. *Nat Rev Mol Cell Biol* **15**, 225–242 (2014).
77. Ashton, N. W. & Cove, D. J. The isolation and preliminary characterisation of auxotrophic and analogue resistant mutants of the moss, Physcomitrella patens. *Molec. Gen. Genet.* **154**, 87–95 (1977).
78. Collonnier, C. *et al.* CRISPR-Cas9-mediated efficient directed mutagenesis and RAD 51-dependent and RAD 51-independent gene targeting in the moss Physcomitrella patens. *Plant Biotechnology Journal* **15**, 122–131 (2017).
79. Yamada, M., Miki, T. & Goshima, G. Imaging Mitosis in the Moss Physcomitrella patens. in *The Mitotic Spindle: Methods and Protocols* (eds. Chang, P. & Ohi, R.) 263–282 (Springer, 2016). doi:10.1007/978-1-4939-3542-0_17.
80. Nakaoka, Y. *et al.* An inducible RNA interference system in Physcomitrella patens reveals a dominant role of augmin in phragmoplast microtubule generation. *Plant Cell* **24**, 1478–1493 (2012).
81. Yi, P. & Goshima, G. Rho of Plants GTPases and Cytoskeletal Elements Control Nuclear Positioning and Asymmetric Cell Division during Physcomitrella patens Branching. *Current Biology* **30**, 2860-2868.e3 (2020).
82. Uchida, M., Ohtani, S., Ichinose, M., Sugita, C. & Sugita, M. The PPR-DYW proteins are required for RNA editing of rps14, cox1 and nad5 transcripts in Physcomitrella patens mitochondria. *FEBS Lett* **585**, 2367–2371 (2011).
83. Galotto, G. *et al.* Myosin XI drives polarized growth by vesicle focusing and local enrichment of F-actin in Physcomitrium patens. *Plant Physiology* **187**, 2509–2529 (2021).

Figure legends

Fig. 1 *ARK* disruption causes severe growth defects

(A) Phylogenetic analysis of *ARK*: moss *Physcomitrium patens* (Pp), Brassica *Arabidopsis thaliana* (At), and liverwort *Marchantia polymorpha* (Mp). Amino acid sequences were collected from the database (accession numbers are listed in the Methods section), aligned with MAFFT, and gaps were deleted. The phylogenetic tree was constructed using the neighbour-joining method and MEGAX software, and its reliability was assessed using 1,000 bootstrapping trials. The bar indicates 0.05 amino acid substitutions per site.

(B) Representative images of 5-week-old moss colonies regenerated from a single protoplast (top row), 6-day-old protonemata (second row), gametophores and rhizoids

863 (third row, where rhizoids are marked with red arrowheads), and the leaf surface
864 (bottom row). The mosses used in this experiment were control (mCherry-α-tubulin),
865 Δ*ARKabc*, Δ*ARKabcd*, and overexpression/rescue lines (Δ*ARKabc*/ARKb-mNG OX
866 and Δ*ARKabc*/ARKb (T169N) -mNG OX). Scale bars: 1 mm (top row), 200 μm
867 (second row), 1 mm (third row), and 100 μm (bottom).
868 (C) Colony area comparison. Colonies were cultured from a single protoplast for three
869 weeks on BCDAT medium. The same moss lines as those in (B) were used in this
870 experiment. The mean area (mm^2) was 41.0 ± 2.28 (control, ±SEM, n = 30), 4.91 ±
871 0.267 (Δ*ARKabc*, ±SEM, n = 45), 30.7 ± 2.42 (Δ*ARKabc*/ARKb-mNG OX, ±SEM, n
872 = 18), 4.26 ± 0.501 (Δ*ARKabc*/ARKb (T169N) -mNG OX, ±SEM, n = 18), 1.90 ±
873 0.188 (Δ*ARKabcd*, ±SEM, n = 49). P-values were calculated using Tukey's multiple
874 comparison test; P < 0.0000001 (control - Δ*ARKabc*), P < 0.0000001 (Δ*ARKabc* -
875 Δ*ARKabc*/ARKb-mNG OX).
876
877 **Fig. 2 ARK transports multiple organelles in protonemal cells**
878 (A) Movement of the nuclei and chloroplasts in protonemal apical cells. The onset time
879 of anaphase was set to 0 min. The yellow circles indicate the positions of the nuclei.
880 Yellow boxes are highlighted in (D). Images were acquired with z-stacks and
881 processed using maximum z-projection: 3 μm × 3 (control mCherry-α-Tubulin line)
882 or 2.5 μm × 3 sections (Δ*ARKabc* and Δ*ARKabc*/ARKb-mNG OX). Bar, 20 μm.
883 (B) Nuclear movement before and after apical cell division. The temporal change in the
884 distance between the nucleus and the cell plate (set at position 0) was plotted with
885 SEM. n = 9 cells (control), n = 10 cells (Δ*ARKabc*), n = 10 cells (Δ*ARKabc*/ARKb-
886 mNG OX).
887 (C) Comparison of the relative position of the metaphase plate of the spindle in dividing
888 apical cells. The relative position was determined by dividing the distance between
889 the metaphase plate and the basal cell wall by that between the cell tip and the basal
890 cell wall. mCherry-α-tubulin was used as the control. The mean relative position was
891 62.2 ± 0.930% (control, ±SEM, n = 10), 41.7 ± 1.71% (Δ*ARKabc*, ±SEM, n = 10),
892 58.3 ± 0.880% (Δ*ARKabc*/ARKb-mNG OX, ±SEM, n = 11), 42.1 ± 1.67%
893 (Δ*ARKabc*/ARKb (T169N) -mNG OX, ±SEM, n = 5). P-values were calculated using
894 Tukey's multiple comparison test; P < 0.0000001 (control - Δ*ARKabc*), P <
895 0.0000001 (Δ*ARKabc* - Δ*ARKabc*/ARKb-mNG OX).
896 (D) Movement of individual chloroplasts 88–96 min after anaphase onset. Yellow boxes
897 in (A) are highlighted. Scale bar, 5 μm.
898 (E) Relative intensity of chloroplasts in apical cells 150 min after anaphase onset.
899 Chloroplast accumulation near the basal cell wall was observed in Δ*ARKabc* and
900 Δ*ARKabc*/ARKb (T169N) -mNG OX plants. mCherry-α-tubulin was used as the
901 control. The quantification methods are described in the Methods section.
902 (F) Bidirectional motility of mitochondria on a microtubule in the control line (mCherry-
903 α-Tubulin/γ-F1ATPase-mNG). The right panel shows the kymograph. Scale bars: 1
904 μm (horizontal) and 30 s (vertical). The growing microtubule end (i.e. the plus end)
905 is indicated by an arrow.
906 (G) Frequency of tip-directed motility of mitochondria in interphase apical cells. The
907 quantification method has been described in the Methods section. The mean
908 frequency was 90.3 ± 4.33% (control, ± SEM, n = 12 cells), 52.8 ± 8.42% (Δ*ARKabc*,

± SEM, n = 12 cells). P-values were calculated using Welch's two-sample t-test; P = 0.001067.

Fig. 3 ARK promotes the movement of RabA2b-marked secretory vesicles

(A) and (B) Accumulation of mNG-RabA2b at the cell tip was reduced in Δ*ARKabc*. mCherry-α-tubulin/RabA2b-mNG was used as control. Scale bar, 5 μm. The mean intensity in (B) was 1.22 ± 0.0845 (control, ±SEM, *n* = 15), 0.69 ± 0.0507 (Δ*ARKabc*, ±SEM, *n* = 12), and 0.970 ± 0.0645 (Δ*ARKabc*/ARKb-mNG OX, ±SEM, *n* = 7). P-values were calculated using Tukey's multiple comparison test; P = 0.0000215 (control - Δ*ARKabc*), P = 0.0704068 (Δ*ARKabc* - Δ*ARKabc*/ARKb-mNG OX).

(C) Representative images of RabA2b-positive vesicles (arrowheads) and number of motile RabA2b-positive vesicles in the absence of microtubules or actin. Scale bar, 5 μm. The number of mNG puncta moving >10 μm in a minute was counted in each cell. The mean number was 2.1 ± 0.46 (control, ±SEM, *n* = 10 cells), 0.0± 0.0 (10 μM oryzalin, ±SEM, *n* = 5 cells), 0.3 ± 0.20 (25 μM latrunculin A, ±SEM, *n* = 10 cells), 0.0± 0.0 (10 μM oryzalin + 25 μM latrunculin A, ±SEM, *n* = 10 cells).

(D) Number of RabA2b-positive vesicles moving for >10 μm in a minute. mCherry-α-tubulin/RabA2b-mNG was used as control. The mean number was 2.3 ± 0.30 (control, ±SEM, *n* = 20 cells), 1.1 ± 0.31 (Δ*ARKabc*, ± SEM, *n* = 17 cells), 2.8 ± 0.60 (Δ*ARKabc*/ARKb-mNG OX, ±SEM, *n* = 17 cells). P-values were calculated using Tukey's multiple comparison test; P = 0.1998938 (control - Δ*ARKabc*), P = 0.0144199 (Δ*ARKabc* - Δ*ARKabc*/ARKb-mNG OX).

Fig. 4 ARKb-mNG shows processive motility *in vivo*

(A) Localisation of ARKb-mNG on endoplasmic microtubules in protonemal cells. Giant green signals near the scale bar represent autofluorescent chloroplasts. Scale bar, 5 μm.

(B) Processive movement of ARKb-mNG along a microtubule. Arrowheads indicate ARKb-mNG signals. Scale bar, 500 nm.

(C) Kymographs of ARKb-mNG (left) and ARKb (T169N)-mNG (right) on microtubules. Scale bar: 5 μm (horizontal) and 5 s (vertical).

(D) Velocity and run length of moving ARKb-mNG signals. Mean values were 572 ± 243 nm/s (velocity, mean ±SD, *n* = 115) and 986 ± 416 nm (run length, mean ±SD, *n* = 106).

Fig. 5 Cell tip growth was severely suppressed in the absence of ARK

(A) Representative images of protonemal cells. The plasma membrane was visualised using FM4-64. The mCherry-α-tubulin line was used as the control. Δ*ARKabcd* exhibited additional nuclear signals derived from the mCherry-tagged histone. Scale bar, 100 μm.

(B) Comparison of subapical cell length. The mean length was 122 ± 4.83 μm (control, ±SEM, *n* = 12), 70.2 ± 2.67 μm (Δ*ARKabc*, ±SEM, *n* = 13), 137 ± 3.97 μm (Δ*ARKabc*/ARKb-mNG OX, ±SEM, *n* = 13). P-values were calculated using Tukey's multiple comparison test; P < 0.0000001 (control - Δ*ARKabc*), P < 0.0000001 (Δ*ARKabc* - Δ*ARKabc*/ARKb-mNG OX).

(C) Comparison of tip growth rates of caulonemal filament. The mCherry-α-tubulin line was used as the control. The mean rate was 20.8 ± 0.962 μm/h (control, ±SEM, *n* =

30), 10.5 ± 0.455 µm/h (Δ*ARKabc*, ±SEM, *n* = 29), 22.1 ± 1.10 µm/h (Δ*ARKabc*/ARKb-mNG OX, ±SEM, *n* = 18), 8.23 ± 0.56 µm/h (Δ*ARKabc*/ARKb (T169N) -mNG OX, ±SEM, *n* = 13). P-values were calculated by Tukey's multiple comparison test; P < 0.0000001 (control - Δ*ARKabc*), P < 0.0000001 (Δ*ARKabc* - Δ*ARKabc*/ARKb-mNG OX).

(D) Representative images of actin foci at the cell tip. Scale bar, 5 µm.

(E) Frequency of actin focusing. The mean frequencies were 68.8 ± 5.84% (Δ*ARKabc*, ±SEM, *n* = 9), 83.6 ± 5.56% (Δ*ARKabc* / ARKb-mNG OX, ±SEM, *n* = 9). P-values were calculated using Welch's two-sample t-test: P = 0.08485 (Δ*ARKabc* - Δ*ARKabc*/ARKb-mNG OX).

(F) Comparison of actin growth rates near the cell tip. F-actin was visualised using Lifeact-mNG. The mean rate was 1.79 ± 0.0790 µm/sec (Δ*ARKabc*, ±SEM, *n* = 14), 2.07 ± 0.084 µm/sec (Δ*ARKabc*/ARKb-mNG OX, ±SEM, *n* = 23). The P-value was calculated using Welch's two-sample t-test: P = 0.02227 (Δ*ARKabc* - Δ*ARKabc*/ARKb-mNG OX).

Fig. 6 ARK and microtubules are necessary for the tip localisation of RopGEFs

(A) and (B) RopGEF3 and RopGEF6 levels at the cell tip were decreased in the *ARK* mutant. (A) Representative images of RopGEF3-mNG and RopGEF6-mNG at the cell tip. Scale bar, 5 µm. (B) Comparison of the intensity of RopGEF3-mNG and RopGEF6-mNG at the cell apex. The mean intensity of RopGEF3-mNG was 1.82 ± 0.202 (control, ±SEM, *n* = 6), 1.20± 0.0792 (Δ*ARKabc*, ±SEM, *n* = 7). P-values were calculated using Welch's two-sample t-test; P = 0.0119944 (control - Δ*ARKabc*). The mean intensity of RopGEF6-mNG was 1.85 ± 0.0905 (control, ±SEM, *n* = 7), 1.23 ± 0.0825 (Δ*ARKabc*, ±SEM, *n* = 10). P-values were calculated using Welch's two-sample t-test: P = 0.0003975 (control - Δ*ARKabc*), P = 0.0000050 (Δ*ARKabc* - Δ*ARKabc*/ARKb-mNG OX).

(C) and (D) Representative images and comparison of For2A-mNG intensity at the cell tip. The mean intensity was 1.03 ± 0.0978 (control, ±SEM, *n* = 10) and 0.802 ± 0.0647 (Δ*ARKabc*, ±SEM, *n* = 11). The P-value was calculated using Welch's two-sample t-test; P = 0.06873 (control - Δ*ARKabc*).

(E) Motor-RopGEF-fusion constructs used in this study. Tailless ARKb and mNeonGreen-FLAG were fused to the N-terminal and C-terminal sides of RopGEF3, respectively. Scale bar: 100 amino acids.

(F) Representative images of Δ*ARKabc* moss expressing native or motor-fused RopGEF3 (ARKb(ΔTail)-RopGEF3-mNG). Top row: 5-week-old moss colonies grown from a single protoplast; second row: 6-day-old protonemata; third row: tip localisation of the fusion protein. Scale bars: 2 mm (top row), 200 µm (second row), and 5 µm (third row).

(G) Relative intensity of chloroplasts along the apical cell at 150 min after anaphase onset. Chloroplast accumulation near the basal cell wall observed in Δ*ARKabc* was not rescued by the fusion RopGEF3 construct.

(H) Area comparison of 5-week-old moss colonies. Colonies were cultured on BCDAT medium from a single protoplast for five weeks. The mean area (mm^2) was 28.2 ± 2.42 (Δ*ARKabc*, ±SEM, *n* = 18), 50.5 ± 3.08 (Δ*ARKabc*/RopGEF3-mNG OX, ±SEM, *n* = 18), 91.5 ± 4.41 (Δ*ARKabc*/ARKb(Δtail)-RopGEF3-mNG, ±SEM, *n* = 18). P-

values were calculated using Tukey's multiple comparison test; P = 0.1878188 (Δ*ARKabc* - Δ*ARKabc*/RopGEF3-mNG OX), P < 0.0000001 (Δ*ARKabc* - Δ*ARKabc*/ARKb-RopGEF3-mNG).

Fig. 7 AtARK2 and AtARK3 expression partially rescues moss Δ*ARKabc*

(A) Representative images of 5-week-old moss colonies regenerated from a single protoplast (top) and 6-day-old protonemata (bottom). Scale bars: 2 mm (top) and 200 µm (bottom).

(B) Representative images of protonemal apical cells. Arrowheads and white lines indicate the positions of the nucleus and the cell plate, respectively. Scale bar, 100 µm.

(C) Relative intensity of chloroplasts along the apical cell at 150 min after anaphase onset (±SEM). The basal accumulation of chloroplasts in Δ*ARKabc* was abolished after the ectopic expression of AtARK2 but not of AtARK3.

(D) Model for microtubule-dependent transport in *Physcomitrium patens* protonemal cells. Giant organelles, such as nuclei and chloroplasts, are transported to the plus and minus ends of the microtubules by ARK and kinesin-14s (KCH and KCBP), respectively (i.e. tug-of-war). ARK also transports secretory vesicles, which are presumably passed to myosin XI at the cell tip for exocytosis [83]. The proteins and cell wall materials required for tip growth are also candidate cargos for ARK, as ARK depletion severely suppresses polarised cell growth.

Supplemental Fig. 1 Establishment of *Physcomitrium patens ARK* mutants

(A) Representative images of 3-week-old moss colonies of *ARK* mutants. mCherry-α-tubulin was used as a control. Scale bar, 5 mm.

(B) Sequencing revealed frameshift mutations in the Δ*ARKabc* and Δ*ARKabcd* sequences used in this study (displayed as SnapGene sequence files).

Supplemental Fig. 2 *ARK* deletion does not affect microtubule dynamics

(A) Comparison of microtubule dynamics. Upper row, control (mCherry-α-tubulin) and Δ*ARKabc*; lower row, control (GFP-α-tubulin/Histone-mCherry), and Δ*ARKabcd.* The mean ± SEM, number of samples, and P-values are shown in Table S1.

(B) Comparison of microtubule orientation in apical cells based on EB1-Citrine tracking. The quantification method is described in the Methods section. The frequency of tip-directed movement (%) was 97.0 ± 1.16 (mCherry-α-Tubulin, ±SEM, n = 18) and 88.5 ± 2.61 (Δ*ARKabc*, ±SEM, n = 8). The P-value was calculated using Welch's two-sample t-test; P = 0.007365.

Supplemental Fig. 3 The truncation-rescue assay reveals the essentiality of ARM repeats

(A) Truncated ARKb-mNG constructs used in this experiment. The protein domains were predicted using NCBI's conserved domain database (https://www.ncbi.nlm.nih.gov/Structure/cdd/wrpsb.cgi) and SMART (http://smart.embl.de).

(B) Area comparison of 3-week-old moss colonies. Colonies were cultured from a single protoplast for three weeks on BCDAT medium. The datasets of Δ*ARKabc*/FL (full-

1048 length) are identical to those shown in Fig. 1C. The mean area (mm^2) was 4.88 ±
1049 0.651 (Δ*ARKabc*/ΔARM, ±SEM, *n* = 18), 7.04 ± 1.07 (Δ*ARKabc*/ΔTail, ±SEM, *n* =
1050 18).
1051 (C) Relative intensity of chloroplasts along the apical cell at 150 min after anaphase onset.
1052 The chloroplasts remained accumulated near the basal cell wall after the expression
1053 of the ΔARM or ΔTail construct.
1054
1055 **Supplemental Fig. 4 *ARK* deletion affects cell length, but not the cell cycle duration**
1056 **or Rop4 localisation**
1057 (A) Comparison of cell cycle durations. The mean duration (h) was 7.43 ± 0.307 (control,
1058 ±SEM, *n* = 24), 7.58 ± 0.232 (Δ*ARKabc*, ±SEM, *n* = 13), 6.93 ± 0.220
1059 (Δ*ARKabc*/ARKb-mNG OX, ±SEM, *n* = 36).
1060 (B) Comparison of tip growth rates in the presence of 500 pM or 50 nM latrunculin A
1061 (LatA). The mCherry-α-tubulin line was used for drug treatment. The mean rate
1062 (μm/h) was 9.69 ± 1.20 (Δ*ARKabc*, ±SEM, *n* = 5), 23.0 ± 1.00 (control [+0.5%
1063 DMSO], ±SEM, *n* = 5), 16.7 ± 1.20 (+500 pM LatA, ±SEM, *n* = 6), 9.64 ± 0.702 (+50
1064 nM LatA, ±SEM, *n* = 17).
1065 (C) and (D) Representative images and comparison of intensities of functional Rop4-
1066 mNG at the cell tip. The mean intensity was 1.29 ± 0.0724 (control, ±SEM, *n* = 6),
1067 1.54 ± 0.140 (Δ*ARKabc*, ±SEM, *n* = 11).
1068 (E) The apical accumulation of RopGEF3 and RopGEF6 depends on the microtubules.
1069 Snapshots of the same cell before and 50-min after oryzalin addition are shown.
1070 DMSO was used as a control. mCherry-α-tubulin-expressing RopGEF3-mNG or
1071 RopGEF6-mNG was used in this experiment. Scale bar, 5 μm.
1072 (F) Temporal changes in RopGEF3-mNG or RopGEF6-mNG intensity at the cell tip after
1073 drug addition. A decrease in localisation was observed after microtubule disruption
1074 with oryzalin. Intensities relative to those before drug treatment are plotted (±SEM, *n*
1075 = 6–13).
1076
1077 **Supplemental Fig. 5 RNAi of *ARKd* in Δ*ARKabc* causes abnormal outgrowth**
1078 (A) Representative image sequences of abnormal cell growth after *ARKd* RNAi induction
1079 by β-estradiol. Left, outgrowth in the apical cell; right, outgrowth in the subapical
1080 cell. Scale bars, 100 μm.
1081 (B) Comparison of apical cell shape after 1 μM β-estradiol or control 0.1% DMSO
1082 treatment. The numbers shown in the bar graphs indicate the actual number of counted
1083 cells.
1084
1085 ## Supplemental movie legends
1086
1087 **Movie 1 Overall basal motility of chloroplasts after cell division in Δ*ARKabc***
1088 Time-lapse movie of microtubules (mCherry-α-tubulin, magenta) and chloroplasts
1089 (autofluorescence, cyan) in apical cells after anaphase onset (0.0 min). The bright
1090 magenta signals on the left represent the anaphase spindles and phragmoplasts. White
1091 arrowheads indicate the positions of the nuclei. Control (expressing mCherry-α-tubulin)
1092 and Δ*ARKabc* lines are also shown. Scale bar, 20 μm.
1093

1094 **Movie 2 Motility of ARKb-mNG on cytoplasmic microtubules *in vivo***
1095 Time-lapse movie of ARKb-mNG obtained using oblique illumination fluorescence
1096 microscopy. White arrowheads indicate the puncta of ARKb-mNG that move
1097 processively and unidirectionally on the microtubules. Magenta, tubulin; green, ARKb-
1098 mNG. Scale bar, 5 μm.

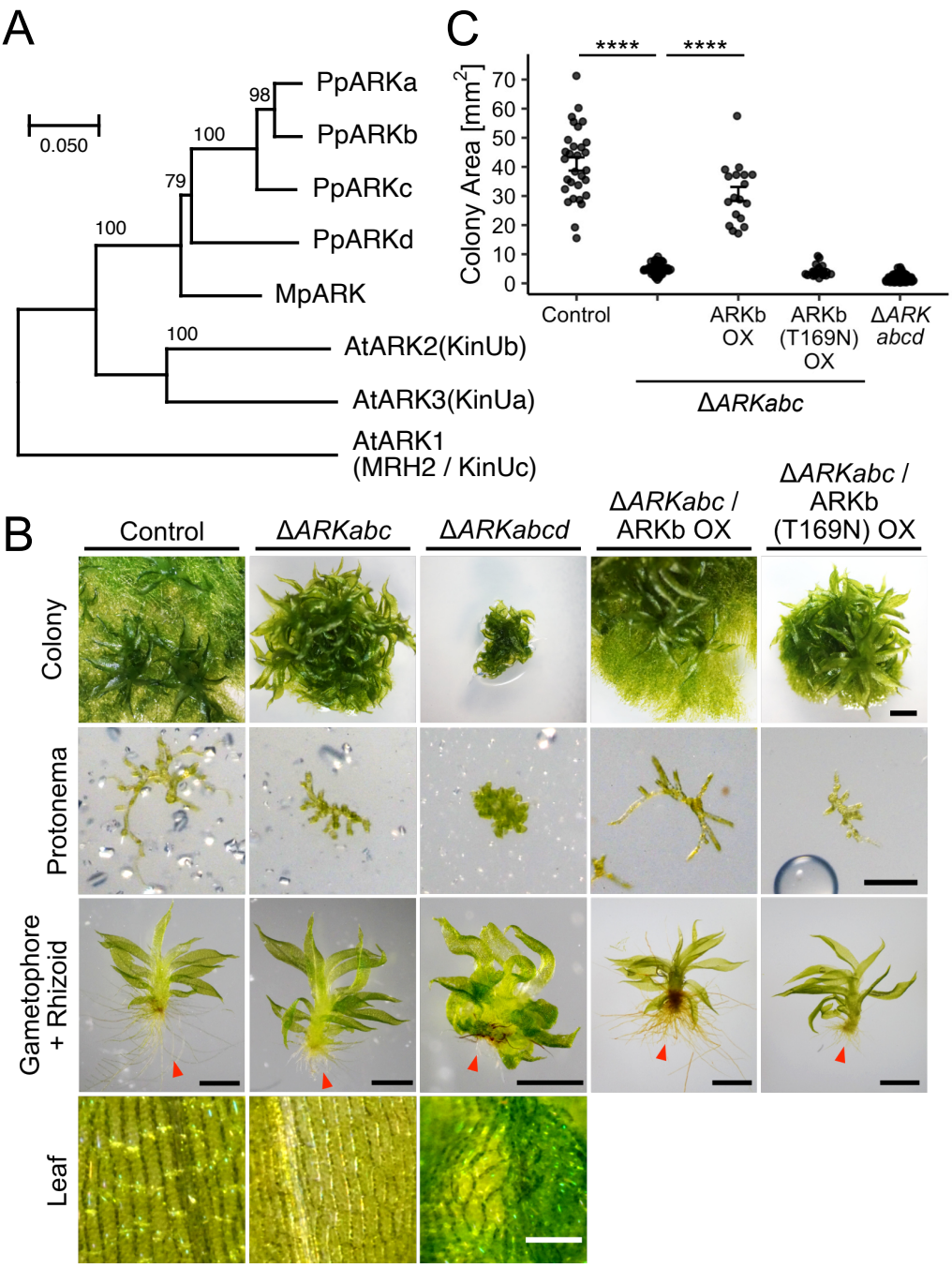

Fig. 1 *ARK* disruption causes severe growth defects

(A) Phylogenetic analysis of *ARK*: moss *Physcomitrium patens* (Pp), Brassica *Arabidopsis thaliana* (At), and liverwort *Marchantia polymorpha* (Mp). Amino acid sequences were collected from the database (accession numbers are listed in the Methods section), aligned with MAFFT, and gaps were deleted. The phylogenetic tree was constructed using the neighbour-joining method and MEGAX software, and its reliability was assessed using 1,000 bootstrapping trials. The bar indicates 0.05 amino acid substitutions per site.

(B) Representative images of 5-week-old moss colonies regenerated from a single protoplast (top row), 6-day-old protonemata (second row), gametophores and rhizoids (third row, where rhizoids are marked with red arrowheads), and the leaf surface (bottom row). The mosses used in this experiment were control (mCherry-α-tubulin), Δ*ARKabc*, Δ*ARKabcd*, and overexpression/rescue lines (Δ*ARKabc*/ARKb-mNG OX and Δ*ARKabc*/ARKb (T169N) -mNG OX). Scale bars: 1 mm (top row), 200 μm (second row), 1 mm (third row), and 100 μm (bottom).

(C) Colony area comparison. Colonies were cultured from a single protoplast for three weeks on BCDAT medium. The same moss lines as those in (B) were used in this experiment. The mean area (mm^2) was 41.0 ± 2.28 (control, ±SEM, n = 30), 4.91 ± 0.267 (Δ*ARKabc*, ±SEM, n = 45), 30.7 ± 2.42 (Δ*ARKabc*/ARKb-mNG OX, ±SEM, n = 18), 4.26 ± 0.501 (Δ*ARKabc*/ARKb (T169N) -mNG OX, ±SEM, n = 18), 1.90 ± 0.188 (Δ*ARKabcd*, ±SEM, n = 49). P-values were calculated using Tukey's multiple comparison test; $P < 0.0000001$ (control - Δ*ARKabc*), $P < 0.0000001$ (Δ*ARKabc* - Δ*ARKabc*/ARKb-mNG OX).

2

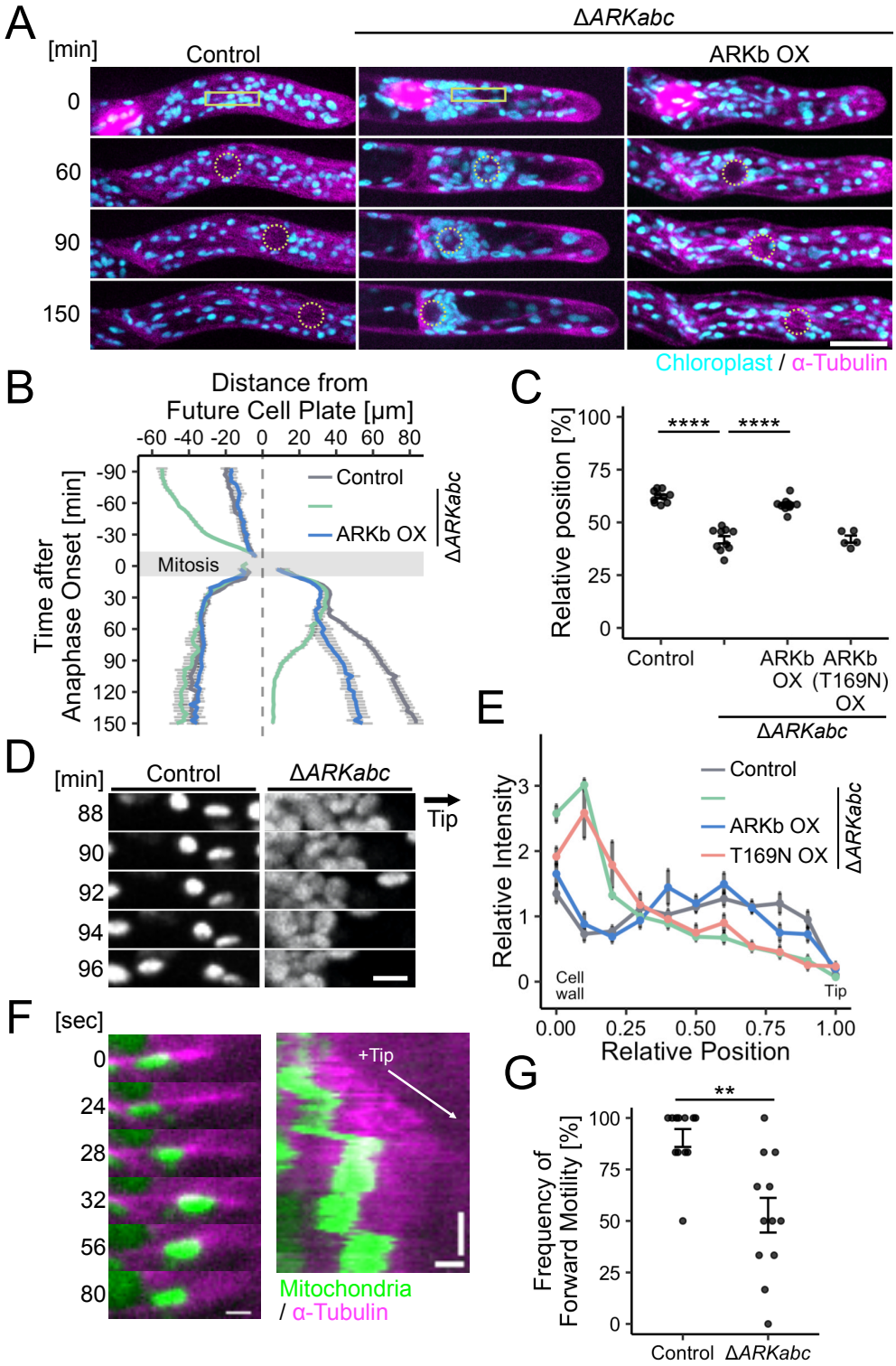

Fig. 2 ARK transports multiple organelles in protonemal cells

(A) Movement of the nuclei and chloroplasts in protonemal apical cells. The onset time of anaphase was set to 0 min. The yellow circles indicate the positions of the nuclei. Yellow boxes are highlighted in (D). Images were acquired with z-stacks and processed using maximum z-projection: 3 μm × 3 (control mCherry-α-Tubulin line) or 2.5 μm × 3 sections (Δ*ARKabc* and Δ*ARKabc*/ARKb-mNG OX). Bar, 20 μm.

(B) Nuclear movement before and after apical cell division. The temporal change in the distance between the nucleus and the cell plate (set at position 0) was plotted with SEM. *n* = 9 cells (control), *n* = 10 cells (Δ*ARKabc*), *n* = 10 cells (Δ*ARKabc*/ARKb-mNG OX).

(C) Comparison of the relative position of the metaphase plate of the spindle in dividing apical cells. The relative position was determined by dividing the distance between the metaphase plate and the basal cell wall by that between the cell tip and the basal cell wall. mCherry-α-tubulin was used as the control. The mean relative position was 62.2 ± 0.930% (control, ±SEM, *n* = 10), 41.7 ± 1.71% (Δ*ARKabc*, ±SEM, *n* = 10), 58.3 ± 0.880% (Δ*ARKabc*/ARKb-mNG OX, ±SEM, *n* = 11), 42.1 ± 1.67% (Δ*ARKabc*/ARKb (T169N) -mNG OX, ±SEM, *n* = 5). P-values were calculated using Tukey's multiple comparison test; P < 0.0000001 (control - Δ*ARKabc*), P < 0.0000001 (Δ*ARKabc* - Δ*ARKabc*/ARKb-mNG OX).

(D) Movement of individual chloroplasts 88–96 min after anaphase onset. Yellow boxes in (A) are highlighted. Scale bar, 5 μm.

(E) Relative intensity of chloroplasts in apical cells 150 min after anaphase onset. Chloroplast accumulation near the basal cell wall was observed in Δ*ARKabc* and Δ*ARKabc*/ARKb (T169N) -mNG OX plants. mCherry-α-tubulin was used as the control. The quantification methods are described in the Methods section.

(F) Bidirectional motility of mitochondria on a microtubule in the control line (mCherry-α-Tubulin/γ-F1ATPase-mNG). The right panel shows the kymograph. Scale bars: 1 μm (horizontal) and 30 s (vertical). The growing microtubule end (i.e. the plus end) is indicated by an arrow.

(G) Frequency of tip-directed motility of mitochondria in interphase apical cells. The quantification method has been described in the Methods section. The mean frequency was 90.3 ± 4.33% (control, ± SEM, n = 12 cells), 52.8 ± 8.42% (Δ*ARKabc*, ± SEM, n = 12 cells). P-values were calculated using Welch's two-sample t-test; P = 0.001067.

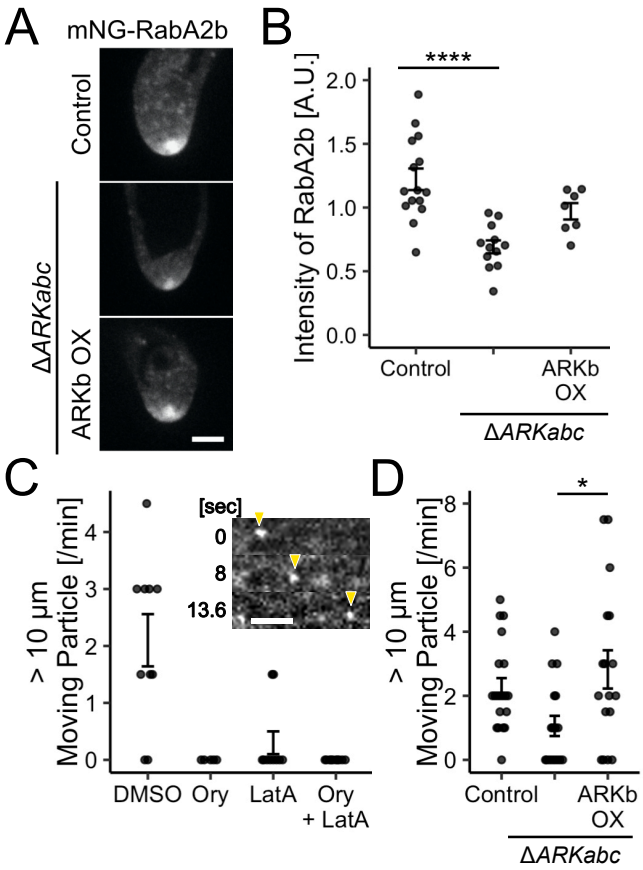

Fig. 3 ARK promotes the movement of RabA2b-marked secretory vesicles

(A) and (B) Accumulation of mNG-RabA2b at the cell tip was reduced in Δ*ARKabc*. mCherry-α-tubulin/RabA2b-mNG was used as control. Scale bar, 5 µm. The mean intensity in (B) was 1.22 ± 0.0845 (control, ±SEM, *n* = 15), 0.69 ± 0.0507 (Δ*ARKabc*, ±SEM, *n* = 12), and 0.970 ± 0.0645 (Δ*ARKabc*/ARKb-mNG OX, ±SEM, *n* = 7). P-values were calculated using Tukey's multiple comparison test; P = 0.0000215 (control - Δ*ARKabc*), P = 0.0704068 (Δ*ARKabc* - Δ*ARKabc*/ARKb-mNG OX).

(C) Representative images of RabA2b-positive vesicles (arrowheads) and number of motile RabA2b-positive vesicles in the absence of microtubules or actin. Scale bar, 5 µm. The number of mNG puncta moving >10 µm in a minute was counted in each cell. The mean number was 2.1 ± 0.46 (control, ±SEM, *n* = 10 cells), 0.0 ± 0.0 (10 µM oryzalin, ±SEM, *n* = 5 cells), 0.3 ± 0.20 (25 µM latrunculin A, ±SEM, *n* = 10 cells), 0.0 ± 0.0 (10 µM oryzalin + 25 µM latrunculin A, ±SEM, *n* = 10 cells).

(D) Number of RabA2b-positive vesicles moving for >10 µm in a minute. mCherry-α-tubulin/RabA2b-mNG was used as control. The mean number was 2.3 ± 0.30 (control, ±SEM, *n* = 20 cells), 1.1 ± 0.31 (Δ*ARKabc*, ± SEM, *n* = 17 cells), 2.8 ± 0.60 (Δ*ARKabc*/ARKb-mNG OX, ±SEM, *n* = 17 cells). P-values were calculated using Tukey's multiple comparison test; P = 0.1998938 (control - Δ*ARKabc*), P = 0.0144199 (Δ*ARKabc* - Δ*ARKabc*/ARKb-mNG OX).

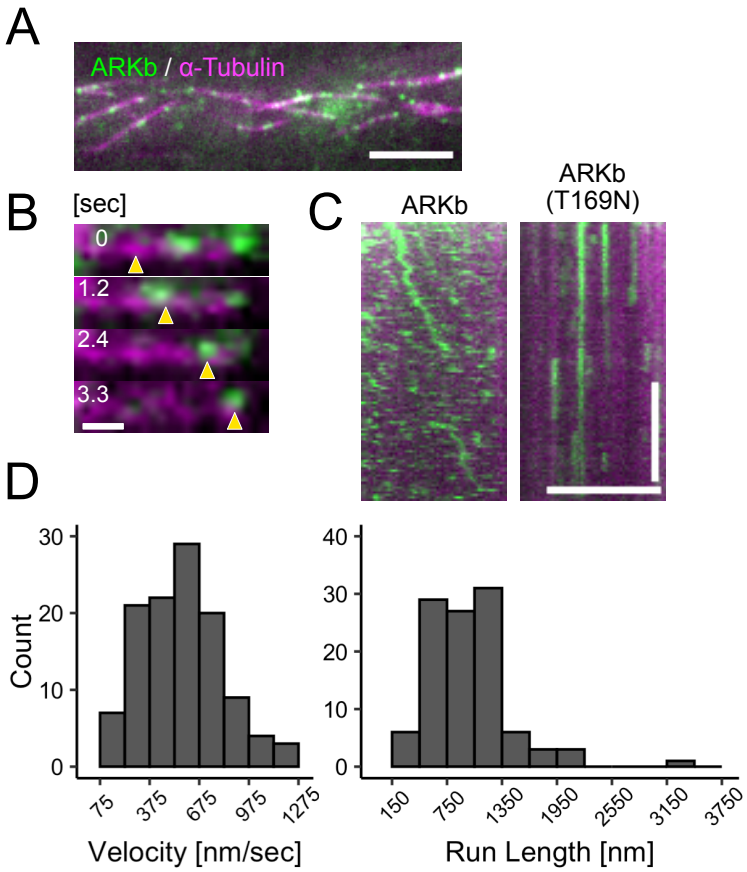

Fig. 4 ARKb-mNG shows processive motility *in vivo*

(A) Localisation of ARKb-mNG on endoplasmic microtubules in protonemal cells. Giant green signals near the scale bar represent autofluorescent chloroplasts. Scale bar, 5 μm.

(B) Processive movement of ARKb-mNG along a microtubule. Arrowheads indicate ARKb-mNG signals. Scale bar, 500 nm.

(C) Kymographs of ARKb-mNG (left) and ARKb (T169N)-mNG (right) on microtubules. Scale bar: 5 μm (horizontal) and 5 s (vertical).

(D) Velocity and run length of moving ARKb-mNG signals. Mean values were 572 ± 243 nm/s (velocity, mean ±SD, n = 115) and 986 ± 416 nm (run length, mean ±SD, n = 106).

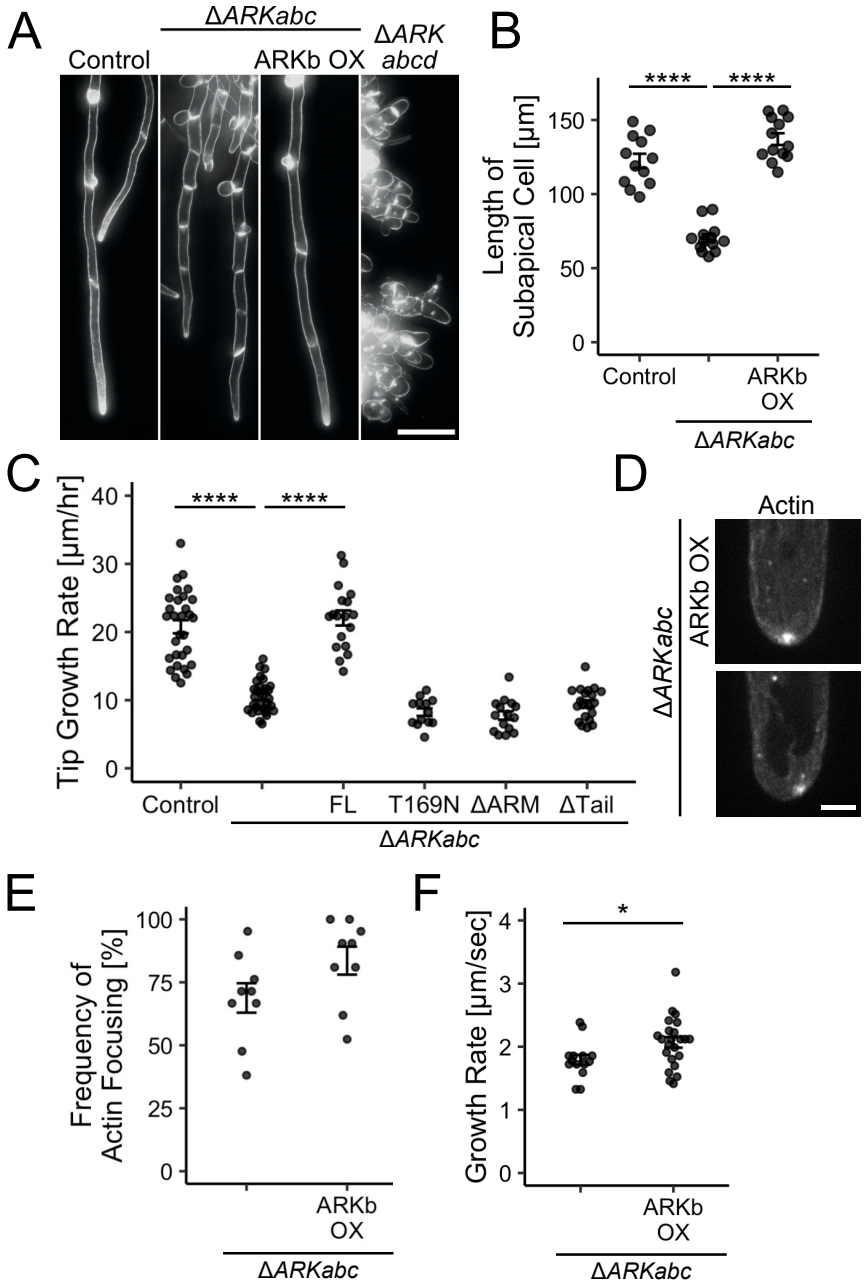

Fig. 5 Cell tip growth was severely suppressed in the absence of ARK

(A) Representative images of protonemal cells. The plasma membrane was visualised using FM4-64. The mCherry-α-tubulin line was used as the control. Δ*ARKabcd* exhibited additional nuclear signals derived from the mCherry-tagged histone. Scale bar, 100 μm.

(B) Comparison of subapical cell length. The mean length was 122 ± 4.83 μm (control, ±SEM, *n* = 12), 70.2 ± 2.67 μm (Δ*ARKabc*, ±SEM, *n* = 13), 137 ± 3.97 μm (Δ*ARKabc*/ARKb-mNG OX, ±SEM, *n* = 13). P-values were calculated using Tukey's multiple comparison test; P < 0.0000001 (control - Δ*ARKabc*), P < 0.0000001 (Δ*ARKabc* - Δ*ARKabc*/ARKb-mNG OX).

(C) Comparison of tip growth rates of caulonemal filament. The mCherry-α-tubulin line was used as the control. The mean rate was 20.8 ± 0.962 μm/h (control, ±SEM, *n* = 30), 10.5 ± 0.455 μm/h (Δ*ARKabc*, ±SEM, *n* = 29), 22.1 ± 1.10 μm/h (Δ*ARKabc*/ARKb-mNG OX, ±SEM, *n* = 18), 8.23 ± 0.56 μm/h (Δ*ARKabc*/ARKb (T169N) -mNG OX, ±SEM, *n* = 13). P-values were calculated by Tukey's multiple comparison test; P < 0.0000001 (control - Δ*ARKabc*), P < 0.0000001 (Δ*ARKabc* - Δ*ARKabc*/ARKb-mNG OX).

(D) Representative images of actin foci at the cell tip. Scale bar, 5 μm.

(E) Frequency of actin focusing. The mean frequencies were 68.8 ± 5.84% (Δ*ARKabc*, ±SEM, *n* = 9), 83.6 ± 5.56% (Δ*ARKabc* / ARKb-mNG OX, ±SEM, *n* = 9). P-values were calculated using Welch's two-sample t-test: P = 0.08485 (Δ*ARKabc* - Δ*ARKabc*/ARKb-mNG OX).

(F) Comparison of actin growth rates near the cell tip. F-actin was visualised using Lifeact-mNG. The mean rate was 1.79 ± 0.0790 μm/sec (Δ*ARKabc*, ±SEM, *n* = 14), 2.07 ± 0.084 μm/sec (Δ*ARKabc*/ARKb-mNG OX, ±SEM, *n* = 23). The P-value was calculated using Welch's two-sample t-test: P = 0.02227 (Δ*ARKabc* - Δ*ARKabc*/ARKb-mNG OX).

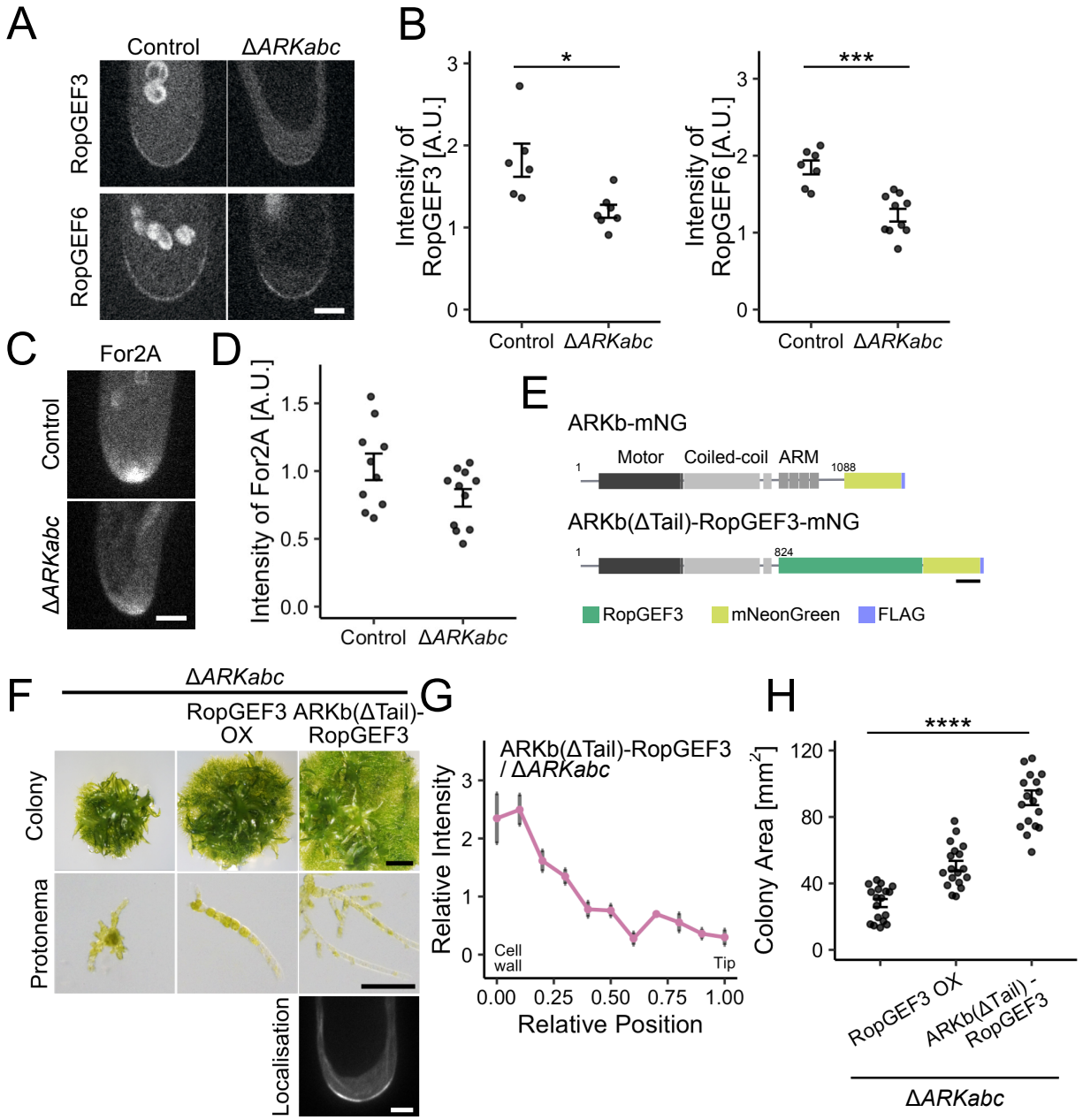

Fig. 6 ARK and microtubules are necessary for the tip localisation of RopGEFs

(A) and (B) RopGEF3 and RopGEF6 levels at the cell tip were decreased in the *ARK* mutant. (A) Representative images of RopGEF3-mNG and RopGEF6-mNG at the cell tip. Scale bar, 5 µm. (B) Comparison of the intensity of RopGEF3-mNG and RopGEF6-mNG at the cell apex. The mean intensity of RopGEF3-mNG was 1.82 ± 0.202 (control, ±SEM, *n* = 6), 1.20 ± 0.0792 (Δ*ARKabc*, ±SEM, *n* = 7). P-values were calculated using Welch's two-sample t-test; P = 0.0119944 (control - Δ*ARKabc*). The mean intensity of RopGEF6-mNG was 1.85 ± 0.0905 (control, ±SEM, *n* = 7), 1.23 ± 0.0825 (Δ*ARKabc*, ±SEM, *n* = 10). P-values were calculated using Welch's two-sample t-test: P = 0.0003975 (control - Δ*ARKabc*), P = 0.0000050 (Δ*ARKabc* - Δ*ARKabc*/ARKb-mNG OX).

(C) and (D) Representative images and comparison of For2A-mNG intensity at the cell tip. The mean intensity was 1.03 ± 0.0978 (control, ±SEM, *n* = 10) and 0.802 ± 0.0647 (Δ*ARKabc*, ±SEM, *n* = 11). The P-value was calculated using Welch's two-sample t-test; P = 0.06873 (control - Δ*ARKabc*).

(E) Motor-RopGEF-fusion constructs used in this study. Tailless ARKb and mNeonGreen-FLAG were fused to the N-terminal and C-terminal sides of RopGEF3, respectively. Scale bar: 100 amino acids.

(F) Representative images of Δ*ARKabc* moss expressing native or motor-fused RopGEF3 (ARKb(ΔTail)-RopGEF3-mNG). Top row: 5-week-old moss colonies grown from a single protoplast; second row: 6-day-old protonemata; third row: tip localisation of the fusion protein. Scale bars: 2 mm (top row), 200 µm (second row), and 5 µm (third row).

(G) Relative intensity of chloroplasts along the apical cell at 150 min after anaphase onset. Chloroplast accumulation near the basal cell wall observed in Δ*ARKabc* was not rescued by the fusion RopGEF3 construct.

(H) Area comparison of 5-week-old moss colonies. Colonies were cultured on BCDAT medium from a single protoplast for five weeks. The mean area (mm^2) was 28.2 ± 2.42 (Δ*ARKabc*, ±SEM, *n* = 18), 50.5 ± 3.08 (Δ*ARKabc*/RopGEF3-mNG OX, ±SEM, *n* = 18), 91.5 ± 4.41 (Δ*ARKabc*/ARKb(Δtail)-RopGEF3-mNG, ±SEM, *n* = 18). P-values were calculated using Tukey's multiple comparison test; P = 0.1878188 (Δ*ARKabc* - Δ*ARKabc*/RopGEF3-mNG OX), P < 0.0000001 (Δ*ARKabc* - Δ*ARKabc*/ARKb-RopGEF3-mNG).

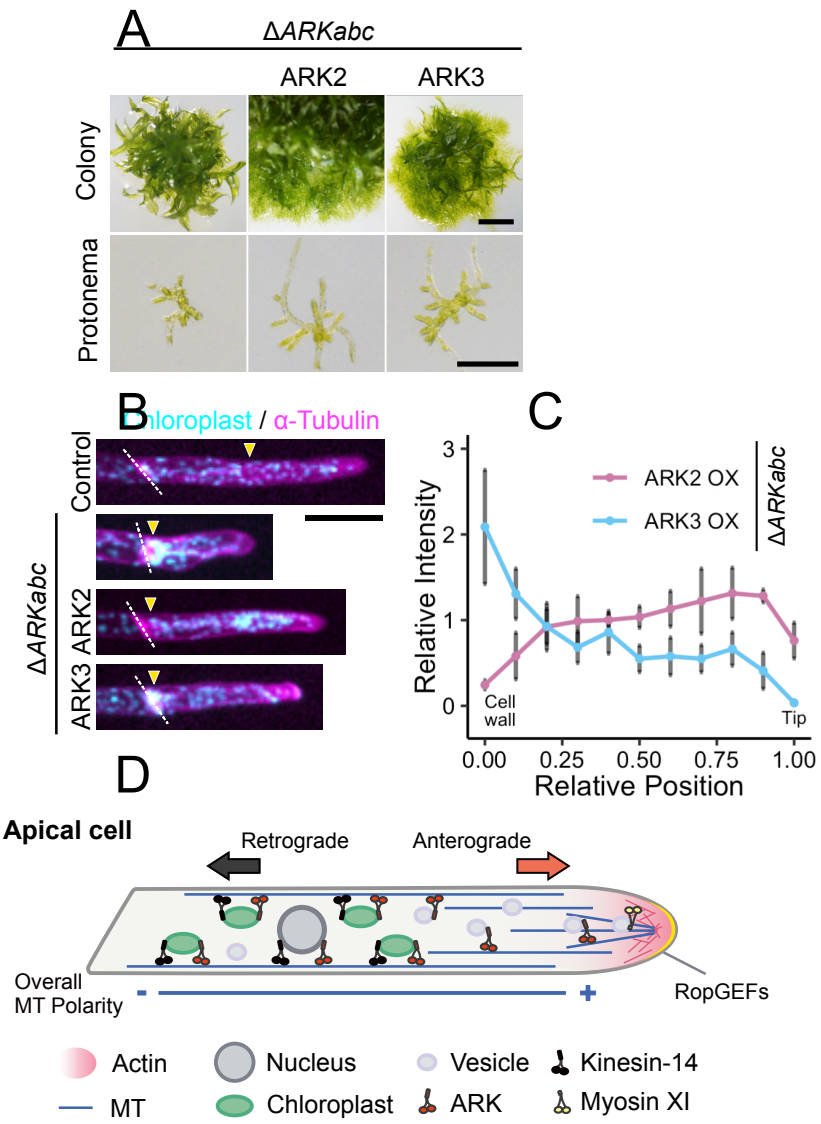

Fig. 7 AtARK2 and AtARK3 expression partially rescues moss Δ*ARKabc*

(A) Representative images of 5-week-old moss colonies regenerated from a single protoplast (top) and 6-day-old protonemata (bottom). Scale bars: 2 mm (top) and 200 μm (bottom).

(B) Representative images of protonemal apical cells. Arrowheads and white lines indicate the positions of the nucleus and the cell plate, respectively. Scale bar, 100 μm.

(C) Relative intensity of chloroplasts along the apical cell at 150 min after anaphase onset (±SEM). The basal accumulation of chloroplasts in Δ*ARKabc* was abolished after the ectopic expression of AtARK2 but not of AtARK3.

(D) Model for microtubule-dependent transport in *Physcomitrium patens* protonemal cells. Giant organelles, such as nuclei and chloroplasts, are transported to the plus and minus ends of the microtubules by ARK and kinesin-14s (KCH and KCBP), respectively (i.e. tug-of-war). ARK also transports secretory vesicles, which are presumably passed to myosin XI at the cell tip for exocytosis [83]. The proteins and cell wall materials required for tip growth are also candidate cargos for ARK, as ARK depletion severely suppresses polarised cell growth.

S1

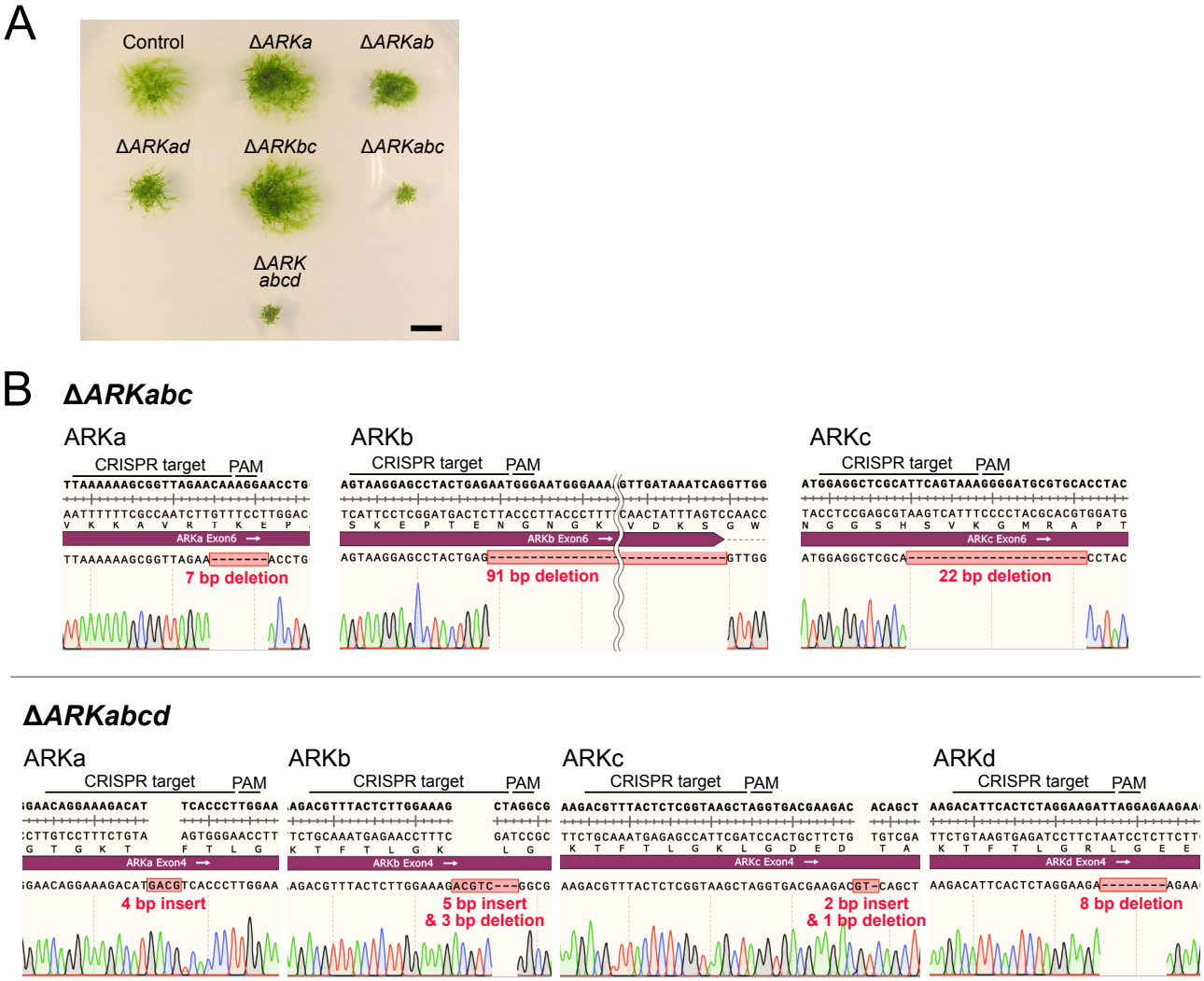

Supplemental Fig. 1 Establishment of *Physcomitrium patens ARK* mutants

(A) Representative images of 3-week-old moss colonies of *ARK* mutants. mCherry-α-tubulin was used as a control. Scale bar, 5 mm.

(B) Sequencing revealed frameshift mutations in the Δ*ARKabc* and Δ*ARKabcd* sequences used in this study (displayed as SnapGene sequence files).

S2

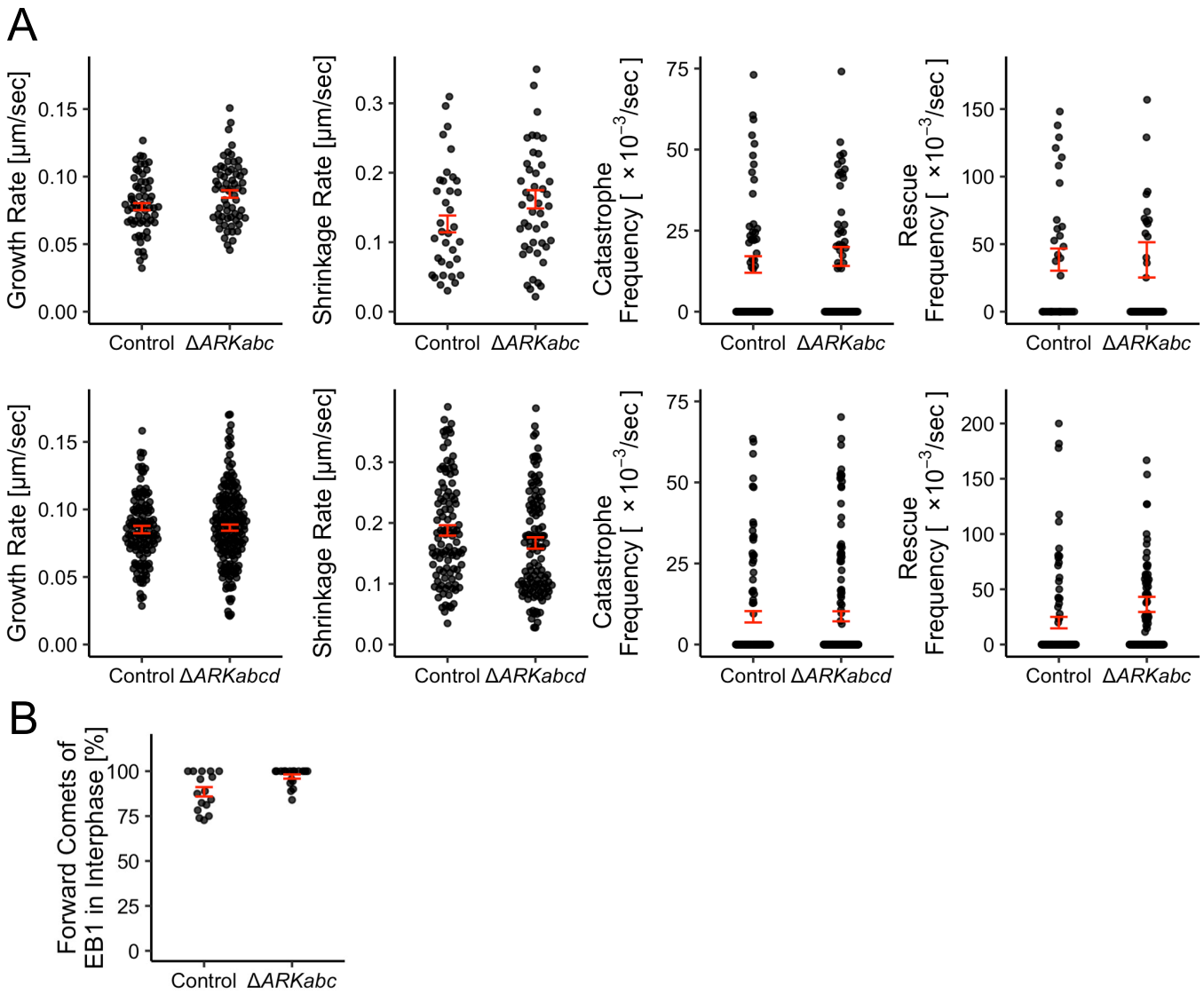

Supplemental Fig. 2 *ARK* deletion does not affect microtubule dynamics

(A) Comparison of microtubule dynamics. Upper row, control (mCherry-α-tubulin) and Δ*ARKabc*; lower row, control (GFP-α-tubulin/Histone-mCherry), and Δ*ARKabcd.* The mean ± SEM, number of samples, and P-values are shown in Table S1.

(B) Comparison of microtubule orientation in apical cells based on EB1-Citrine tracking. The quantification method is described in the Methods section. The frequency of tip-directed movement (%) was 97.0 ± 1.16 (mCherry-α-Tubulin, ±SEM, *n* = 18) and 88.5 ± 2.61 (Δ*ARKabc*, ±SEM, *n* = 8). The P-value was calculated using Welch's two-sample t-test; P = 0.007365.

S3

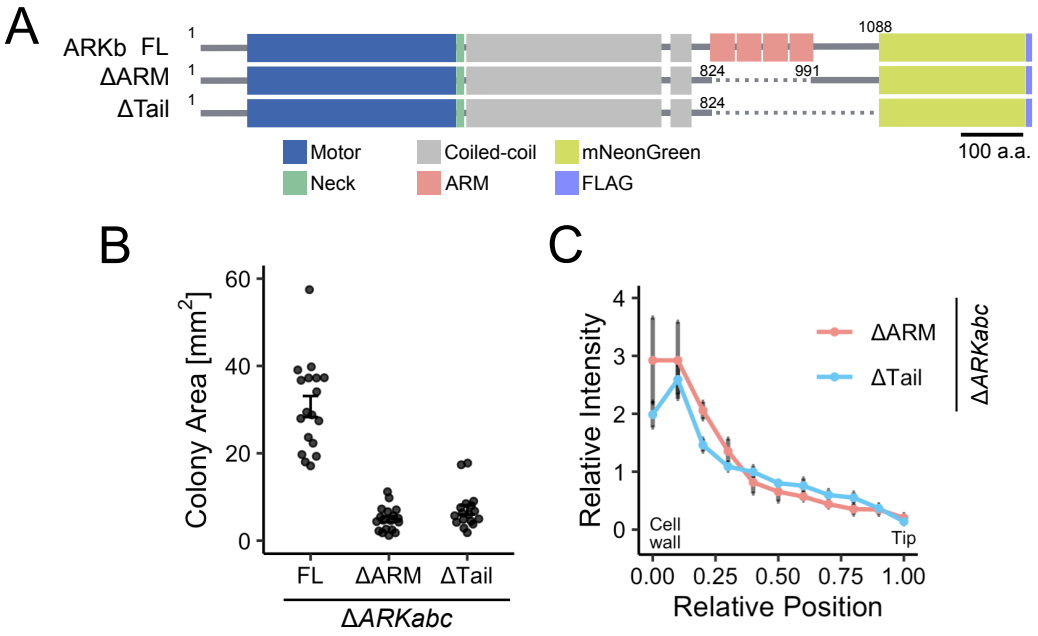

Supplemental Fig. 3 The truncation-rescue assay reveals the essentiality of ARM repeats

(A) Truncated ARKb-mNG constructs used in this experiment. The protein domains were predicted using NCBI's conserved domain database (https://www.ncbi.nlm.nih.gov/Structure/cdd/wrpsb.cgi) and SMART (http://smart.embl.de).

(B) Area comparison of 3-week-old moss colonies. Colonies were cultured from a single protoplast for three weeks on BCDAT medium. The datasets of Δ*ARKabc*/FL (full-length) are identical to those shown in Fig. 1C. The mean area (mm^2) was 4.88 ± 0.651 (Δ*ARKabc*/ΔARM, ±SEM, n = 18), 7.04 ± 1.07 (Δ*ARKabc*/ΔTail, ±SEM, n = 18).

(C) Relative intensity of chloroplasts along the apical cell at 150 min after anaphase onset. The chloroplasts remained accumulated near the basal cell wall after the expression of the ΔARM or ΔTail construct.

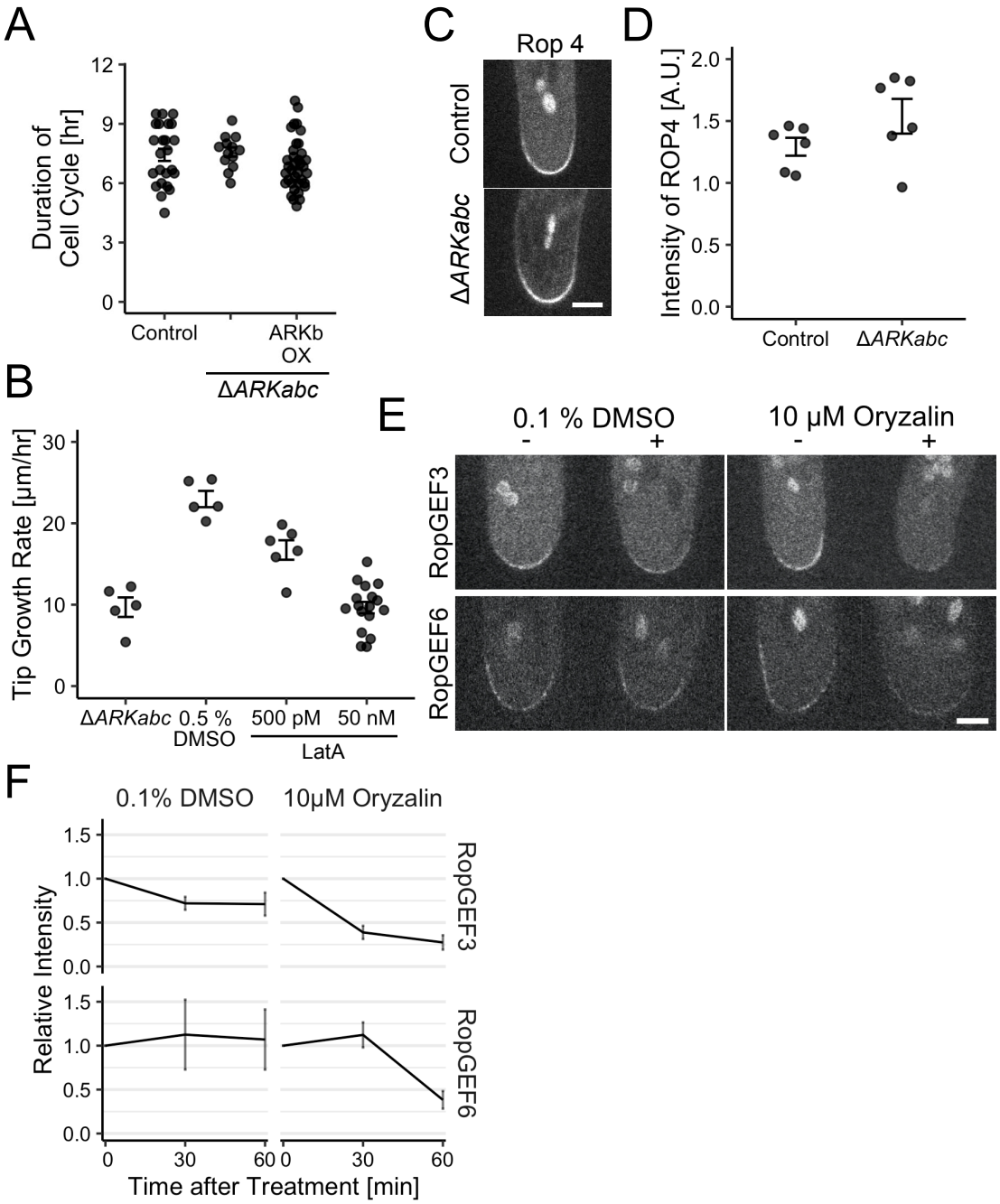

Supplemental Fig. 4 *ARK* deletion affects cell length, but not the cell cycle duration or Rop4 localisation

(A) Comparison of cell cycle durations. The mean duration (h) was 7.43 ± 0.307 (control, ±SEM, *n* = 24), 7.58 ± 0.232 (Δ*ARKabc*, ±SEM, *n* = 13), 6.93 ± 0.220 (Δ*ARKabc*/ARKb-mNG OX, ±SEM, *n* = 36).

(B) Comparison of tip growth rates in the presence of 500 pM or 50 nM latrunculin A (LatA). The mCherry-α-tubulin line was used for drug treatment. The mean rate (µm/h) was 9.69 ± 1.20 (Δ*ARKabc*, ±SEM, *n* = 5), 23.0 ± 1.00 (control [+0.5% DMSO], ±SEM, *n* = 5), 16.7 ± 1.20 (+500 pM LatA, ±SEM, *n* = 6), 9.64 ± 0.702 (+50 nM LatA,± SEM, *n* = 17).

(C) and (D) Representative images and comparison of intensities of functional Rop4-mNG at the cell tip. The mean intensity was 1.29 ± 0.0724 (control, ±SEM, *n* = 6), 1.54 ± 0.140 (Δ*ARKabc*, ±SEM, *n* = 11).

(E) The apical accumulation of RopGEF3 and RopGEF6 depends on the microtubules. Snapshots of the same cell before and 50-min after oryzalin addition are shown. DMSO was used as a control. mCherry-α-tubulin-expressing RopGEF3-mNG or RopGEF6-mNG was used in this experiment. Scale bar, 5 µm.

(F) Temporal changes in RopGEF3-mNG or RopGEF6-mNG intensity at the cell tip after drug addition. A decrease in localisation was observed after microtubule disruption with oryzalin. Intensities relative to those before drug treatment are plotted (±SEM, *n* = 6–13).

S5

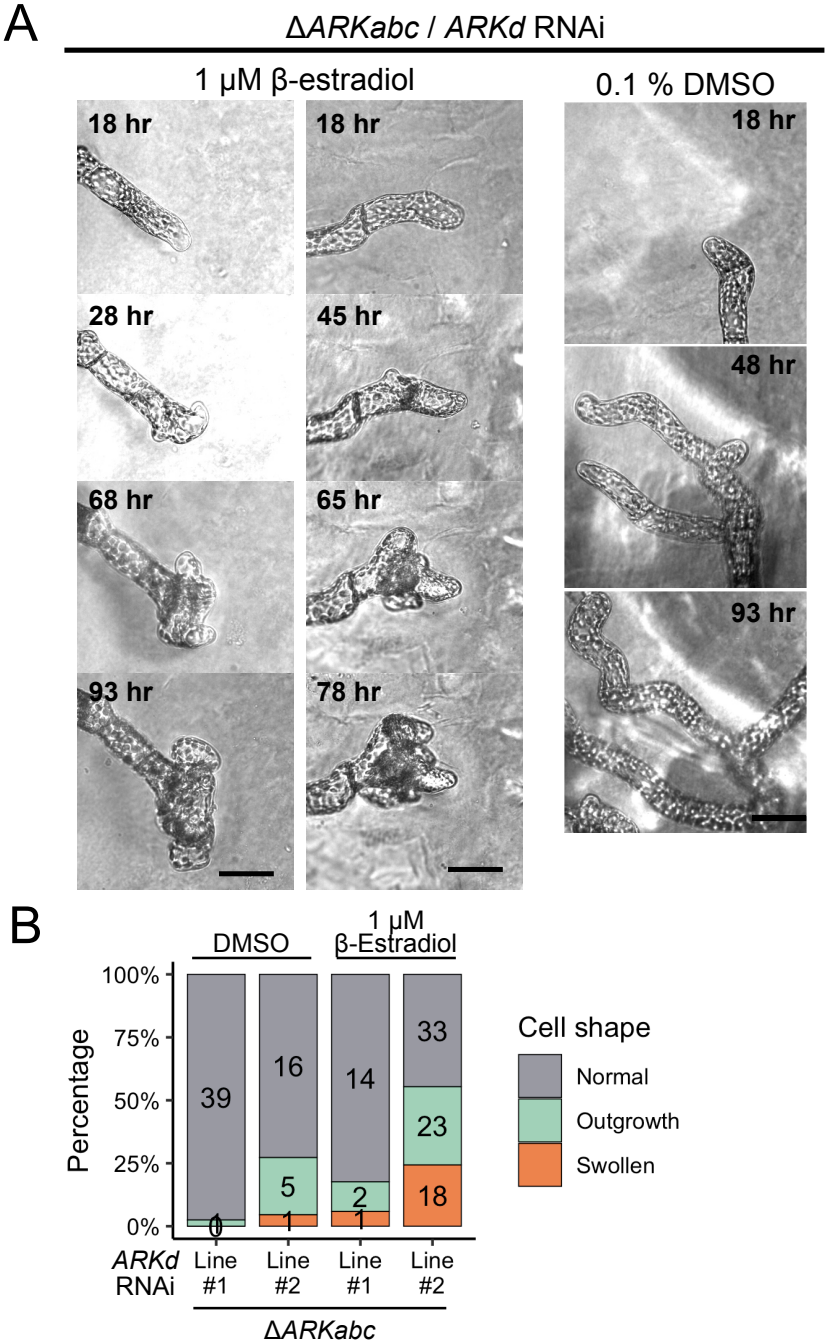

Supplemental Fig. 5 RNAi of *ARKd* in Δ*ARKabc* causes abnormal outgrowth

(A) Representative image sequences of abnormal cell growth after *ARKd* RNAi induction by β-estradiol. Left, outgrowth in the apical cell; right, outgrowth in the subapical cell. Scale bars, 100 μm.

(B) Comparison of apical cell shape after 1 μM β-estradiol or control 0.1% DMSO treatment. The numbers shown in the bar graphs indicate the actual number of counted cells.